Title

Polymorphism in Weberite Na2Fe2F7 and its Effects on Electrochemical Properties as a Na-Ion Cathode

Journal

Chemistry of Materials, 35(9)

ISSN

0897-4756

Authors

Foley, Emily E
Wu, Vincent C
Jin, Wen
et al.

Publication Date

2023-05-09

DOI

10.1021/acs.chemmater.3c00233

Polymorphism in Weberite $Na_2Fe_2F_7$ and its Effects on Electrochemical Properties as a Na-ion Cathode

Emily E. Foley,[1,2] Vincent C. Wu,[1,2] Wen Jin,[2,3] Wei Cui,[2,4] Eric Yoshida,†[1,2] Alexis Manche, ‡[1] Raphaële J. Clément[1,2*]

[1]Materials Department, University of California Santa Barbara, California 93106, USA

[2]Materials Research Laboratory, University of California Santa Barbara, California 93106, USA

[3]Chemical Engineering Department, University of California Santa Barbara, California 93106, USA

[4]Physics Department, University of California Santa Barbara, California 93106, USA

†Present address: Materials Department, University of California Irvine, California 92697, USA

‡Present address: School of Chemistry, University of St-Andrews, North Haugh, St-Andrews, KY16 9ST, UK

*Corresponding author email: rclement@ucsb.edu

Abstract

Weberite-type sodium transition metal fluorides ($Na_2M^{2+}M'^{3+}F_7$) have emerged as potential high performance sodium intercalation cathodes, with predicted energy densities in the 600-800 Wh/kg range and fast Na-ion transport. One of the few weberites that has been electrochemically tested is $Na_2Fe_2F_7$, yet inconsistencies in its reported structure and electrochemical properties have hampered the establishment of clear structure-property relationships. In this study, we reconcile structural characteristics and electrochemical behavior using a combined experimental-computational approach. First principles calculations reveal the inherent metastability of weberite-type phases, the close energetics of several $Na_2Fe_2F_7$ weberite polymorphs, as well as their predicted (de)intercalation behavior. We find that as-prepared $Na_2Fe_2F_7$ samples inevitably contain a mixture of polymorphs, with local probes such as solid-state nuclear magnetic resonance and Mössbauer spectroscopy providing unique insights into the distribution of Na and Fe local environments. Polymorphic $Na_2Fe_2F_7$ exhibits a respectable initial capacity yet steady capacity fade, a consequence of the transformation of the $Na_2Fe_2F_7$ weberite phases to the more stable perovskite-type $NaFeF_3$ phase upon cycling, as revealed by *ex situ* synchrotron X-ray diffraction and solid-state NMR. Overall, these findings highlight the need for greater control over weberite polymorphism and phase stability through compositional tuning and synthesis optimization.

Introduction

Batteries are found in nearly every facet of modern life, including in portable electronics, electric vehicles, and large-scale energy storage systems, largely enabled by lithium-ion batteries (LIBs). However, with the imminent materials supply shortage caused by the ever increasing reliance on lithium (Li), nickel (Ni), and cobalt (Co) to produce Li-ion cathodes, more sustainable battery chemistries are needed. When considering possible electrode chemistries, sodium (Na)- and iron (Fe)-based compounds stand out as promising candidates. However, the higher atomic weight and larger ionic radius of Na^+ compared to Li^+, as well as the 0.3 V higher potential of the Na^+/Na redox couple compared to Li^+/Li, leads to inherently lower theoretical energy densities for sodium-ion batteries (SIBs) compared to their Li-ion analogues. While significant work has gone towards developing layered oxide,[1–3] polyanion,[4–6] and Prussian Blue[7,8] cathodes for SIBs, viable Na alternatives to current Li systems have proven elusive.[9] A paradigm shift in the development of competitive Na cathodes hinges on the investigation of new structural frameworks and anion chemistries.

Fluorine substitution has been shown to increase the operating voltage (and thereby the energy density) of both oxide[10,11] and polyanion-based[12,13] cathodes due to the inductive effect introduced by the highly electronegative F^- anion. However, pure transition metal fluorides are infrequently used as cathodes due to their generally poor ionic and electronic conduction properties.[14–17] While electronic conduction can be partially mitigated by carbon-coating, particle downsizing, and nanostructuring[18–20], ionic conduction is an intrinsic requirement for a topotactic Na (de)intercalation process. For poor ionic conductors, structure-preserving Na extraction and reinsertion processes are replaced by decomposition or conversion reactions. Conversion reactions should in theory result in high capacities but are poorly reversible in practice[21,22]: they have been reported for cryolite-like Na_3MF_6,[23] rutile MF_2[24,25], and for perovskite-type MF_3[14,26,27] and $NaMF_3$[28,29] on deep discharge. Clearly, transition metal fluoride structures containing fast Na-ion transport pathways are needed. In this regard, weberite compounds (with general formula $Na_2M^{2+}M'^{3+}F_7$) have been shown to exhibit an open framework structure that holds promise for facile Na-ion diffusion and topotactic Na-ion (de)intercalation.[30–32]

Weberite-type sodium transition metal fluorides have been studied for their magnetic properties since the 1970s[33,34], but have only been explored as Na-ion battery electrode materials over the past few years.[30–32,35,36] In 2019, Euchner *et al.* predicted, using first principles calculations, that this material class should lead to good Na-ion diffusion properties, high Na insertion potentials, and high capacities, resulting in energy densities competitive with common Li-ion cathode materials.[35] A recent experimental report by Park *et al.* demonstrated exceptional performance for the $Na_2Fe_2F_7$ weberite cathode, including an initial capacity of 184 mAh/g at C/20, and an outstanding full cell capacity retention of 88.3% at 2C (initial capacity of 118 mAh/g) after 1000 cycles.[30] While $Na_2Fe_2F_7$ remains the best performing weberite cathode to date,[30] other chemistries such as Na_2TiFeF_7[31] and Na_2MVF_7 (M = Mn, Fe, Co)[32] have been shown to result in capacities in excess of 185 and 147 mAh/g, respectively.

While Park *et al.* reported a trigonal $Na_2Fe_2F_7$ weberite,[30] two other variants of the weberite structure (orthorhombic and monoclinic) have been reported for this compound,[20,28] indicating a complex phase stability landscape for $Na_2Fe_2F_7$, with direct impacts on its applicability as an intercalation electrode. Here, we report an in-depth computational-experimental investigation of the structure, phase stability, and electrochemistry of $Na_2Fe_2F_7$, aiming to establish clear links between local and long-range structural features and Na intercalation properties. We find that $Na_2Fe_2F_7$ is prone to polymorphism, with all three weberite forms present in our samples despite extensive synthesis optimization, as evidenced by synchrotron X-ray diffraction (SXRD), and supported by ^{57}Fe Mössbauer and ^{23}Na solid-state nuclear

magnetic resonance (ss-NMR) spectroscopy. Notably, this is the first NMR investigation of a weberite material (supplemented with first principles calculations of NMR parameters) and provides key insights into the Na local environments. From an electrochemical performance standpoint, we highlight both the promise presented and difficulties faced by weberite cathodes such as $Na_2Fe_2F_7$. While density functional theory (DFT) calculations reveal that all three $Na_2Fe_2F_7$ polymorphs are capable of exchanging 2 Na-ions per formula unit (compositions between $NaFe_2F_7$ and $Na_3Fe_2F_7$) through a solid-solution mechanism on charge and discharge, kinetic limitations on deep discharge limit the practical capacity, which may be related to the large predicted volume expansion at high Na contents. We further identify a phase transformation upon cycling, revealed by *ex situ* SXRD and ^{23}Na ss-NMR. While this study confirms the suitability of weberites as potential high energy cathode materials for SIBs, it also highlights a need for controlled synthesis routes to obtain single-phase weberite samples, for the optimization of electrode preparation methods to achieve the full redox capacity of $Na_2Fe_2F_7$ and related systems, and for a better understanding of the metastability issues facing this class of cathode materials.

Results & Discussion

Weberite Structure and its Variants

The weberite structure is a fluorine-deficient superstructure of fluorite (CaF_2) with general formula $A_2B_2X_7$, where A and B are cations and X is an anion. The high symmetry variant (*Imma* space group) and A site local environments are shown in **Figures 1a-c** for the weberite mineral, Na_2MgAlF_7. Weberites retain the same cationic face-centered cubic stacking sequence as fluorite, but as they are anion-deficient the B cations are now only 6-fold coordinated, while the A cations retain the 8-fold coordination typical of the fluorite structure. The mixed-valence B cations, $B1$ and $B2$ (typically divalent M^{2+} and trivalent M^{3+} metals, respectively), form a network of three-dimensional corner-connected octahedra composed of one-dimensional chains of $B1$ octahedra that are connected to each other by $B2$ octahedra. The A cations occupy distorted cubic sites ($A1$, **Figure 1b**) and bihexagonal pyramidal sites ($A2$, **Figure 1c**). The $A1$ polyhedra form edge-sharing chains that also share edges with the $A2$ corner-connected polyhedral chains, creating a three-dimensionally connected A cation network. Additionally, the weberite structure can be viewed as alternating close-packed cation layers of A_3B and AB_3, as shown in **Figure S1**. In each layer, the majority cation species (e.g. A in A_3B) forms a Kagomé-type network, and the minority cation species occupies the center of the Kagomé rings.

Several weberite variants have been reported, that differ in their stacking sequence of the Kagomé-like layers. A nomenclature system has been proposed by Grey et al.[38] based on the crystal system and number of close-packed cation slabs (*e.g.*, a pair of A_3B and AB_3 layers) within the unit cell. For example, the high symmetry weberite variant (shown in **Figure 1a**) is denoted $2O$ as it is based on the orthorhombic crystal system and the smallest repeating unit contains two cation slabs. Na-M-F weberites reported to date form the $2O$ (*Imma*), $2M$ (monoclinic $C2/c$), $3T$ (trigonal $P3_121$), and/or $4M$ (monoclinic $C2/c$) structures, where the different slab stackings can be summarized as *AA* for $2O$, *ABAB* for $2M$, *AABBAABB* for $4M$, and *ABCABC* for $3T$. Structural diagrams that illustrate those differences are shown in **Figure S2**. We note that the $2M$ variant has only been reported for Na_2CuGaF_7 and we do not consider this variant further in this work.

$Na_2Fe_2F_7$ Polymorphism and Energetics

Given the structural diversity of weberites, a detailed investigation of possible $Na_2Fe_2F_7$ polymorphism and its impact on electrochemical properties is warranted if this material is to be considered for SIB applications.

In 1993, a single crystal XRD study by Yakubovich *et al.* suggested that $Na_2Fe_2F_7$ crystallizes in the 4*M* weberite variant,[37] in line with prior reports of the 4*M* structure for other Fe^{2+}-based weberites.[33,39,40] Yet, more recently, Dey *et al.*[36] and Park *et al.*[30] reported the synthesis of the 2*O* and 3*T* variants of $Na_2Fe_2F_7$, respectively, as well as their electrochemical properties in Na-ion cells. Those contrasting reports are difficult to reconcile, especially since they either do not include any diffraction data,[37] or they include patterns with significantly broadened reflections[30,36] and that lack both the sensitivity and resolution to distinguish between the very similar diffraction patterns of the 4*M*, 2*O*, and 3*T* polymorphs (see simulated patterns in **Figure S3**). The main differences between those patterns lie in the splitting of select peaks, and a few low intensity peaks characteristic of the 3*T* and 4*M* structures. Thus, in order to identify the weberite structural variant(s) present in a given sample using XRD, high quality data on highly crystalline materials – if not single crystals – is necessary.

To gain insight into the likelihood of obtaining the various weberite structural variants of $Na_2Fe_2F_7$, the phase stability of Na-Fe-Fe compounds was investigated. The formation energy of each polymorph, as well as competing phases, was calculated using DFT, with the resultant NaF-FeF_2-FeF_3 ternary diagram shown in **Figure 1d** (values in **Table S1**). Within this space, the weberite polymorphs and $Na_5Fe_3F_{14}$ are metastable, lying 5 to 15 meV/atom above the hull, while the most stable phase is Na_3FeF_6, lying on the hull. As illustrated in **Figure 1e**, the energy above the hull for each weberite polymorph is within 5 meV/atom of each other, suggesting that all three of the polymorphs may be stabilized at room temperature. These DFT results, as well as the multiple polymorphs previously reported for $Na_2Fe_2F_7$, suggest that X-ray diffraction patterns for $Na_2Fe_2F_7$ weberites should be analyzed with care and complemented with local structure characterization to identify the polymorph(s) present in a given sample.

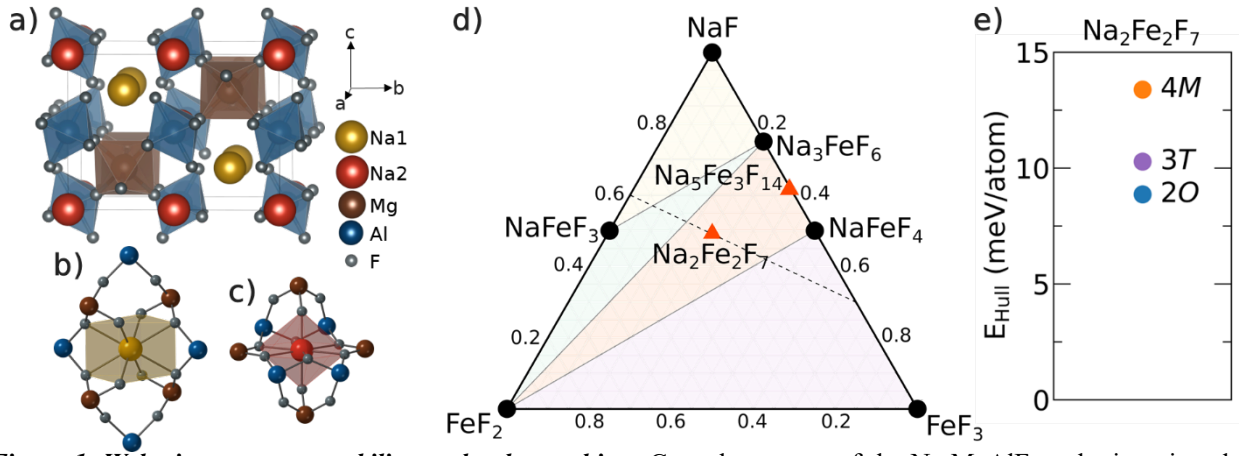

Figure 1, Weberite structure, stability, and polymorphism. Crystal structure of the Na_2MgAlF_7 weberite mineral, highlighting the MF_6 (where *M* = Mg, Al) polyhedral network in **a)**, and the local Na coordination environments: Na1 in distorted cubic sites in **b)**, and Na2 in bihexagonal pyramidal sites in **c)**. **d)** DFT-predicted NaF-FeF_2-FeF_3 ternary phase diagram, where stable compounds are shown as black circles, metastable compounds as orange triangles, and regions of phase coexistence are shaded. The black, dotted tie-line represents the compositional evolution of the weberite at various stages of charge. **e)** Energy above the hull for the three $Na_2Fe_2F_7$ weberite variants.

Synthesis and Long-range Structural Characterization of $Na_2Fe_2F_7$

$Na_2Fe_2F_7$ was prepared using a mechanochemically assisted solid-state synthesis procedure adapted from Park *et al.*[30] Several annealing temperatures were tested, and the laboratory powder diffraction patterns obtained on the as-prepared samples are shown in **Figure S4**. While Park *et al.* utilized an annealing temperature of 650°C, we found that this temperature resulted in a large amount of impurities (namely, Na_3FeF_6 and FeF_2). In contrast, an annealing temperature of 500°C minimized the amount of impurity phases and was used for the remainder of this study. The SXRD pattern collected on the 500°C annealed

sample and its corresponding Rietveld refinement are shown in **Figure 2a**. Despite careful optimization of the synthesis conditions, impurity phases were still observed (9.5 wt.% Na_3FeF_6 and 0.9 wt.% FeF_2). The presence of a significant amount of Na_3FeF_6 in our sample can be explained by its very negative formation energy (**Figure 1d**) compared to those of the weberite $Na_2Fe_2F_7$ variants.

The SXRD data collected on $Na_2Fe_2F_7$ was analyzed using a combination of Pawley and Rietveld refinements. Refinements involving a single weberite polymorph resulted in poor fits ($\chi^2 > 3.5$, $R_{WP} > 17\%$) due to the complexity of the experimental peak shapes (**Figure 2a inset**), clearly suggesting the presence of many overlapping diffraction peaks and a mixture of phases. Refinement models using all three weberite polymorphs resulted in much improved refinements, with the best refinement ($\chi^2 = 2.12$, $R_{WP} = 9.75\%$) indicating a sample composition of 4.4 wt.% of the 2*O*, 42.4 wt.% of the 3*T*, and 42.8 wt.% of the 4*M* polymorph. To prevent overfitting the diffraction pattern, site occupancies were not refined and thermal factors were constrained to be equal for each atom type, with detailed Rietveld refinement parameters listed in **Tables S2-3**. An additional refinement was performed without the 2*O* polymorph (**Figure S5**), which resulted in a moderately worse fit ($\chi^2 = 2.16$, $R_{WP} = 9.94\%$), indicating that the 2*O* polymorph is in fact present. Given that a multi-phasic $Na_2Fe_2F_7$ sample was obtained in this work, consistent with the similar energetics of the various $Na_2Fe_2F_7$ polymorphs obtained from first principles (**Figure 1c**), it is possible that previous studies of this material overlooked the presence of multiple phases in their samples.

In preparation for electrochemical testing, the pristine material was ball-milled with carbon to improve its electronic conductivity through both particle size reduction and carbon-coating.[19,41,42] Scanning electron microscopy (SEM) images are shown in **Figures 3a,b inset** for pristine and carbon-coated $Na_2Fe_2F_7$. The pristine $Na_2Fe_2F_7$ sample contains ≈ 1-2 μm particles, while the carbon-coated $Na_2Fe_2F_7$ sample contains ≈ 100 nm particles, indicating successful particle downsizing. The SXRD pattern collected on carbon-coated $Na_2Fe_2F_7$, shown in **Figure 2b**, exhibits significant peak broadening and a poor signal-to-noise ratio, a likely consequence of the small average particle size and the buildup of strain in the material during the ball-milling process. Thus, the sole purpose of the Rietveld refinement was to identify the amount of impurity phases present: this was done using a single weberite phase, 4*M*, with detailed Rietveld refinement parameters listed in **Table S4**. The amount of impurity phases in the carbon-coated sample is similar to that prior to carbon-coating, but with 11.4 wt.% of Na_3FeF_6 and no FeF_2 present. The SXRD pattern collected on carbon-coated $Na_2Fe_2F_7$ also exhibits a series of low intensity, sharp reflections indicated with arrows in **Figure 2b** and likely arising from a minor, high symmetry impurity phase. Despite an extensive search comprising all known binary or ternary phases containing the elements Na, Fe, F, C, Zr, and/or O (with Zr and O arising from the ZrO_2 ball mill jar used here), we are unable to assign those reflections, which can neither be fit using an anisotropic strain model.[43]

Insights into Fe and Na local environments from Mössbauer and solid-state NMR spectroscopy

^{57}Fe Mössbauer spectroscopy was used to characterize the Fe local environments in the pristine and carbon-coated $Na_2Fe_2F_7$ samples. The spectrum collected on pristine $Na_2Fe_2F_7$ is shown in **Figure 3a**. A good fit ($\chi^2 = 1.12$) of this spectrum was obtained using five components (fitting parameters are provided in **Table S5**): two doublets at isomer shifts (δ) of 1.45 and 1.25 mm/s, with quadrupolar splittings (ΔE_Q) of 1.38 and 1.42 mm/s, respectively, assigned to $Fe^{2+}F_6$ in the weberite phases; two doublets at δ = 0.43 and 0.45 mm/s, with ΔE_Q = 0.72 and 0.49 mm/s, respectively, assigned to $Fe^{3+}F_6$ in the weberite phases; and a doublet assigned to Na_3FeF_6 using previously-reported Mössbauer parameters (δ = 0.27 mm/s, ΔE_Q = 0.15 mm/s).[23] The $Fe^{2+}F_6$ and $Fe^{3+}F_6$ signals closely match values obtained for other Fe-containing weberite phases.[36,44–46] The multiple doublets assigned to $Fe^{2+}F_6$ and to $Fe^{3+}F_6$ species indicates a distribution of Fe local environments in the distinct weberite polymorphs. Notably, the $Fe^{2+}F_6$ local environment changes more

than the $Fe^{3+}F_6$ local environment in the various forms of $Na_2Fe_2F_7$, which may account for the larger variation in the isomer shift of $Fe^{2+}F_6$ signals. Integration of the Mössbauer signals leads to an average Fe oxidation state of 2.55+ for the weberite phases resulting in a stoichiometry of $Na_{1.90}Fe^{2.55+}{}_2F_7$ (assuming full F occupation)[47] indicating a slight Na deficiency, in line with the ICP results (**Table S6**).

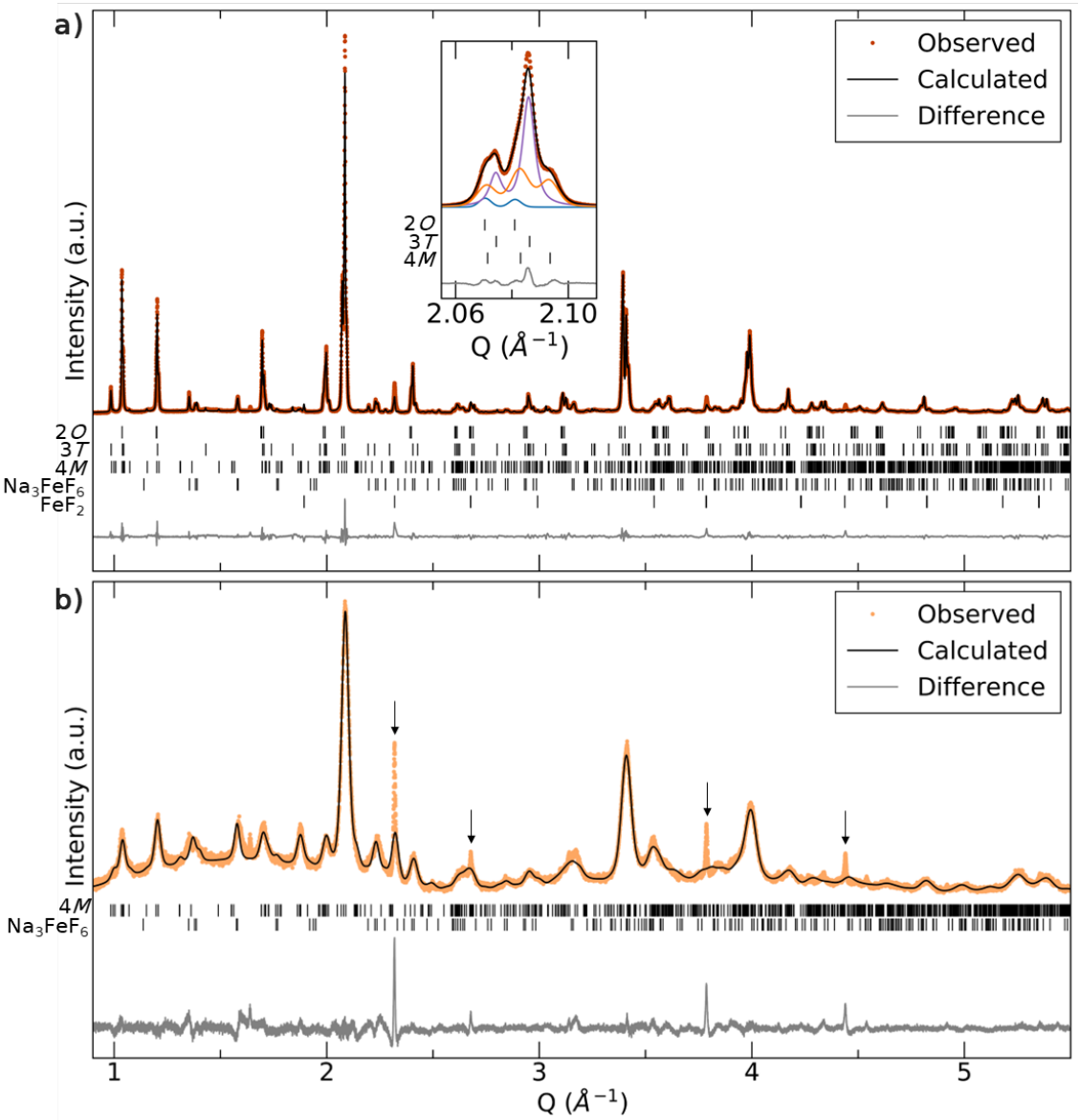

Figure 2. Synchrotron XRD characterization of $Na_2Fe_2F_7$ weberite samples. Synchrotron XRD pattern collected on **a)** pristine and **b)** carbon-coated $Na_2Fe_2F_7$ with their corresponding Rietveld refinements. The inset in **a)** shows an enlarged version of the refinement results for the main weberite peaks, with individual profiles shown for the 2*O* (blue), 3*T* (purple), and 4*M* (orange) polymorphs. The arrows in **b)** indicate reflections associated with an unidentified impurity phase.

The ^{57}Fe Mössbauer spectrum collected on the carbon-coated $Na_2Fe_2F_7$ sample (**Figure 3b**) suggests moderate Fe oxidation upon carbon-coating (average Fe oxidation state of 2.67+). Notably, this spectrum could be fitted with one broad signal for $Fe^{2+}F_6$ and one broad signal for $Fe^{3+}F_6$ (fitting parameters are provided in **Table S5**), indicating greater disorder within the weberite phase(s) upon ball-milling. Overall ^{57}Fe Mössbauer spectroscopy confirms that the weberite material is slightly Na deficient, with this

deficiency increasing upon carbon-coating, resulting in a stoichiometry of about $Na_{1.68}Fe^{2.7+}{}_2F_7$ prior to electrochemical cycling.

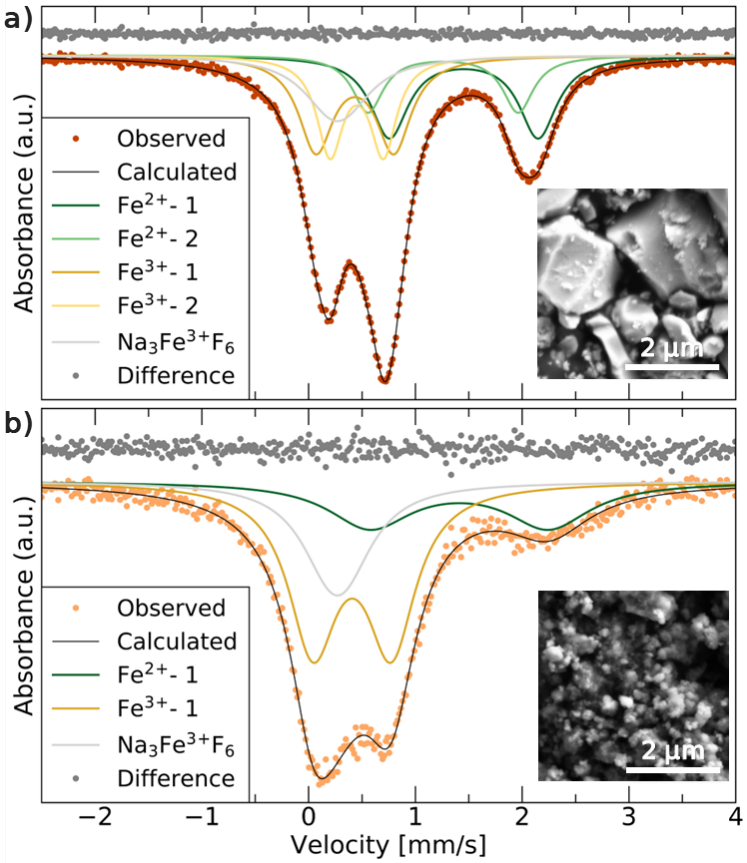

Figure 3. ***^{57}Fe Mössbauer spectroscopy and SEM characterization of $Na_2Fe_2F_7$ weberite samples.*** **a)** ^{57}Fe Mössbauer spectrum and fit collected on **a)** pristine and **b)** carbon-coated $Na_2Fe_2F_7$. The insets show the corresponding SEM micrographs for each material.

The Na local environments in $Na_2Fe_2F_7$ were examined using ^{23}Na ss-NMR. As $Na_2Fe_2F_7$ contains unpaired electrons from the Fe^{2+}/Fe^{3+} species and ^{23}Na is a quadrupolar nucleus (I = 3/2), both paramagnetic and quadrupolar effects are present. These interactions result in significant NMR line broadening and large chemical shifts, leading to significant signal overlap and complicating the attribution of spectral features to specific local environments in the material. Here, the assignment of the complex NMR spectra was assisted by first principles hybrid density functional theory (DFT)/Hartree Fock (HF) calculations of ^{23}Na NMR parameters using the CRYSTAL17 code on the different $Na_2Fe_2F_7$ weberite structural variants (see **Supplementary Note 1** for computational parameters and methodology), with results shown in **Table S7**. The ^{23}Na isotropic chemical shift (δ_{iso}) is dominated by the paramagnetic (Fermi contact) shift resulting from delocalization of unpaired electron spin density from nearby Fe 3*d* orbitals to the ^{23}Na *s* orbital. These paramagnetic interactions also lead to significant spectral broadening. The interaction between the ^{23}Na nuclear quadrupole moment and the electric field gradient (EFG) present at the Na nucleus leads to a further broadening of the spectrum and to a shift of the ^{23}Na resonant frequency due to second-order effects (denoted δ_Q). The observed chemical shift (δ_{obs}) is then the sum of the isotropic Fermi contact shift and of the second-order quadrupolar shift: $\delta_{obs} = \delta_{iso} + \delta_Q$.

Obtaining high resolution spectra of quadrupolar nuclei in paramagnetic materials is complicated by the opposing magnetic field (B_0) dependence of quadrupolar and paramagnetic interactions. While second-

order quadrupolar effects (e.g., δ_Q and associated line broadening) are inversely related to B_0, such that NMR spectra of quadrupolar nuclei are typically obtained at high fields, high field strengths exacerbate paramagnetic broadening and lower fields are preferred for strongly paramagnetic samples. Here, the optimal field strength that maximizes spectral resolution was determined by plotting the predicted δ_{obs} at various magnetic field strengths for cubic and bihexagonal pyramidal Na sites in each weberite polymorph, as shown in **Figure 4a**. The highly asymmetrical bihexagonal pyramidal Na environments exhibit a greater field-dependence of their δ_{obs} due to their larger quadrupolar coupling constants ($C_Q \geq 5$ MHz) compared to cubic Na sites ($C_Q \leq 3.5$ MHz). Our first principles calculations suggest: 1) significant overlap between the ^{23}Na ss-NMR signals associated with cubic Na sites in the 3*T* and 4*M* weberite variants, and similarly for the bihexagonal pyramidal Na signals in those two phases. For the 2*O* polymorph, the resonance associated with the cubic Na environment likely overlaps with those of the bihexagonal pyramidal Na signals from the 3*T* and 4*M* weberite variants, while the signal arising from 2*O* bihexagonal pyramidal Na sites is expected at very negative shifts and should be discernable. 2) At low fields (2.35 T), ^{23}Na signals corresponding to cubic and bihexagonal pyramidal Na sites within a single weberite phase are expected to be separated by nearly 1000 ppm owing to their different second-order quadrupolar shifts (δ_Q), while at higher fields δ_Q becomes negligible and the signals overlap. Thus, to maximally resolve ^{23}Na signals from the different local environments present in the samples of interest, all ^{23}Na ss-NMR spectra were obtained at our lowest field of 2.35 T.

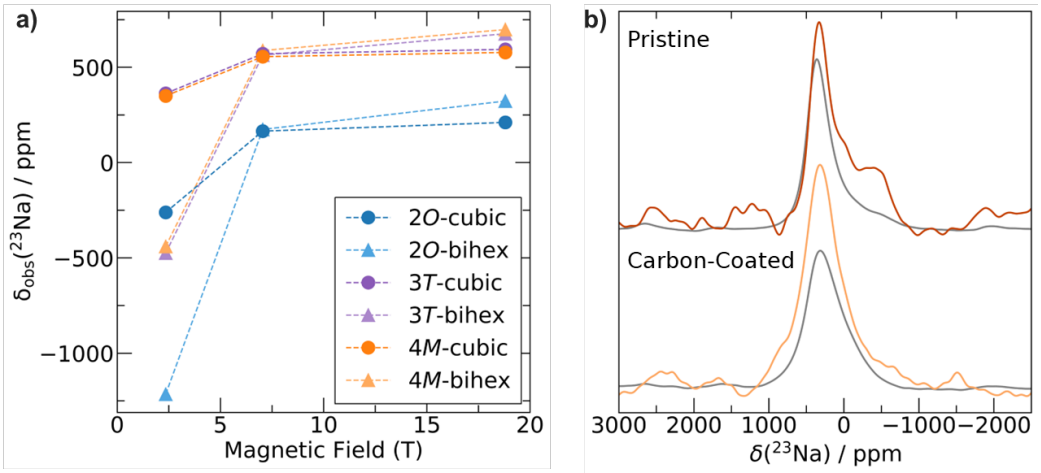

Figure 4. **a)** Field-dependence of the calculated chemical shifts for the average cubic and bihexagonal pyramidal sites in $Na_2Fe_2F_7$ weberite polymorphs. **b)** ^{23}Na ss-NMR spin echo spectra collected on pristine and carbon-coated $Na_2Fe_2F_7$ using $\pi/2$ (grey) and $\pi/6$ (orange) excitation pulses.

^{23}Na ss-NMR spin echo spectra collected on pristine and carbon-coated $Na_2Fe_2F_7$ samples are shown in **Figure 4b**. For each sample, the two overlaid spectra were obtained using a typical $\pi/2$ excitation pulse and a small flip angle ($\pi/6$) excitation pulse, respectively. Despite the decrease in sensitivity caused by the small flip angle, the $\pi/6$ spectra exhibit at least one additional signal at ≈ -400 ppm compared to the $\pi/2$ spectra, that is more prevalent for pristine $Na_2Fe_2F_7$. This additional signal is attributed to bihexagonal pyramidal Na sites, whose larger quadrupolar interactions result in broader, lower intensity signals that are poorly excited by a $\pi/2$ pulse.[48] Thus, the $\pi/2$ spectra are dominated by signals arising from Na in cubic sites, while the $\pi/6$ spectra reflect all Na environments present in the samples. The spectra also contain low intensity signals arising from the Na_3FeF_6 impurity phase, as revealed by the ^{23}Na ss-NMR spin echo spectrum obtained on a Na_3FeF_6 sample overlaid in **Figure S6** with the $\pi/2$ spectra shown in **Figure 4b**. While the 200 ppm Na_3FeF_6 signal is difficult to discern from the $Na_2Fe_2F_7$ phase, the Na_3FeF_6 signal at 1800 ppm is distinguishable but very low in intensity. Finally, while the $\pi/6$ spectra shown in **Figure 4b** could in theory provide some information on the relative population of cubic and

bihexagonal pyramidal Na sites, the strong quadrupolar and paramagnetic interactions present in $Na_2Fe_2F_7$ result in short ^{23}Na ss-NMR signal lifetimes and signal loss over the course of the experiments. Hence, the relative signal intensities in these spectra are not quantitative; besides, measurements of transverse relaxation times (T_2') to account for signal loss are impractical due to their extremely low sensitivity (*e.g.,* the $\pi/6$ spectrum collected on pristine $Na_2Fe_2F_7$ took over 48 h to acquire).

Nearly all the ^{23}Na ss-NMR signals from the weberite variants are predicted to lie within the −500 ppm to 500 ppm range, save from the bihexagonal pyramidal Na resonance and the Na signals arising from the 2*O* variant at more negative shifts (see **Figure 4a**). Clearly, all the main resonances observed in the spectra in **Figure 4b** lie within the expected range for $Na_2Fe_2F_7$ weberites. Yet, the $\pi/6$ spectra show clear differences in the distribution of Na local environments in the pristine and carbon-coated $Na_2Fe_2F_7$ samples. The spectrum collected on the pristine sample exhibits signals at negative shifts (centered around −400 ppm) consistent with the presence of Na in bihexagonal pyramidal sites in the 3*T* and 4*M* phases. Notably, this spectrum appears to contain several overlapping signals, including distinct cubic and bihexagonal pyramidal signals, suggestive of multiple polymorphs present. The carbon-coated sample, however, shows noticeably fewer signals at negative shifts, suggesting that the C-coating process may be reducing the intensity of the quadrupolar interactions and/or reducing the occupation of bihexagonal pyramidal Na sites by introducing more overall disorder into the system.

These results, combined with the previously discussed SXRD and ^{57}Fe Mössbauer data, suggest the preparation of a multi-phasic (predominantly 3*T* and 4*M*) $Na_2Fe_2F_7$ weberite material containing Na_3FeF_6 impurities that partially disorders upon carbon-coating while still retaining the long-range weberite structure.

Electrochemical properties of $Na_2Fe_2F_7$

As the 24 h carbon-coating process affects the weberite structure, several shorter mechanochemical milling times and an *in situ* carbon-coating method were investigated to reduce structural disordering, with results presented in **Supplementary Note 2**. Briefly, none of the alternative carbon-coating methods tested here led to an electrochemical performance on par with that obtained after a 24 h milling step, which was therefore adopted for the remainder of this work.

Results from electrochemical tests on the $Na_2Fe_2F_7$ cathode are presented in **Figure 5**. The voltage profiles for $Na_2Fe_2F_7$ are shown in **Figure 5a** through cycle 50. Unless indicated otherwise, $Na_2Fe_2F_7$ was cycled at a rate of C/20 (full (dis)charge in 20 h assuming the transfer of 2 Na per formula unit) by first charging to 4.3 V vs. Na^+/Na and subsequent cycling between 4.3 V and 1.5 V. Upon first charge, a capacity of 70 mAh/g is achieved with the following discharge providing a reversible capacity of 125 mAh/g. We note that all capacities reported here are calculated assuming that the entire active material is composed of $Na_2Fe_2F_7$. This leads to an underestimation of the capacity attributable to the electrochemically-active phase since SXRD data collected on the pristine, carbon-coated sample suggests the presence of about 10 wt.% of crystalline Na_3FeF_6 impurity that is largely electrochemically-inactive over the potential range probed here. The capacity was computed in this manner as the carbon-coated material likely contains some amount of amorphous electrochemically-active domains, which SXRD is unable to detect. While more Na may be able to intercalate upon discharging the cell to a lower potential, the discharge cutoff voltage was maintained at 1.5 V to prevent the Na_3FeF_6 impurity phase from becoming electrochemically active at lower potentials[23] and interfering with the analysis of the electrochemical behavior of $Na_2Fe_2F_7$. Beyond the first cycle, the capacity fades steadily (**Figure S8a**). Differential capacity (dQ/dV) plots recorded over the first 50 cycles are shown in **Figure 5b**. During the first few cycles, several broad features are observed on charge and discharge, which gradually evolve into two sharp features centered around 3.3/3.6 and 2.8/3.1 V on

discharge/charge. The average discharge voltage (**Figure S8b**) begins at about 2.8 V but gradually fades to 2.7 V, and the charge-discharge voltage hysteresis increases from 0.5 V to 0.75 V after 50 cycles. The rate performance is shown in **Figure 5c**. A respectable capacity of 85 mAh/g is achieved at a rate of C/5, but the capacity quickly drops off as the rate is increased to 1C, suggesting that Na (de)intercalation from/into the weberite cathode is kinetically limited. Galvanostatic intermittent titration technique (GITT) tests were performed to understand the extent of charge-transfer and Na-ion conduction limitations, which additively contribute to the observed overpotential,[49] with results shown in **Figure 5d**. At high and low voltage, large overpotentials (approaching 0.5 V) are observed, while overpotentials are minimal throughout the rest of the electrochemical profile. This suggests that the processes between 2.5 to 4 V, approximately corresponding to Na (de)intercalation and Fe redox between the compositional bounds of $Na_2Fe^{2+}Fe^{3+}F_7$ and $Na_1Fe^{3+}{}_2F_7$, are kinetically facile, while Na (de)intercalation and Fe redox beyond those bounds is hindered. Even after a 2-hour equilibration period after each current pulse, a significant voltage hysteresis remains throughout the electrochemical profile, suggesting some asymmetry associated with the charge-discharge processes, which will be revisited in the following sections.

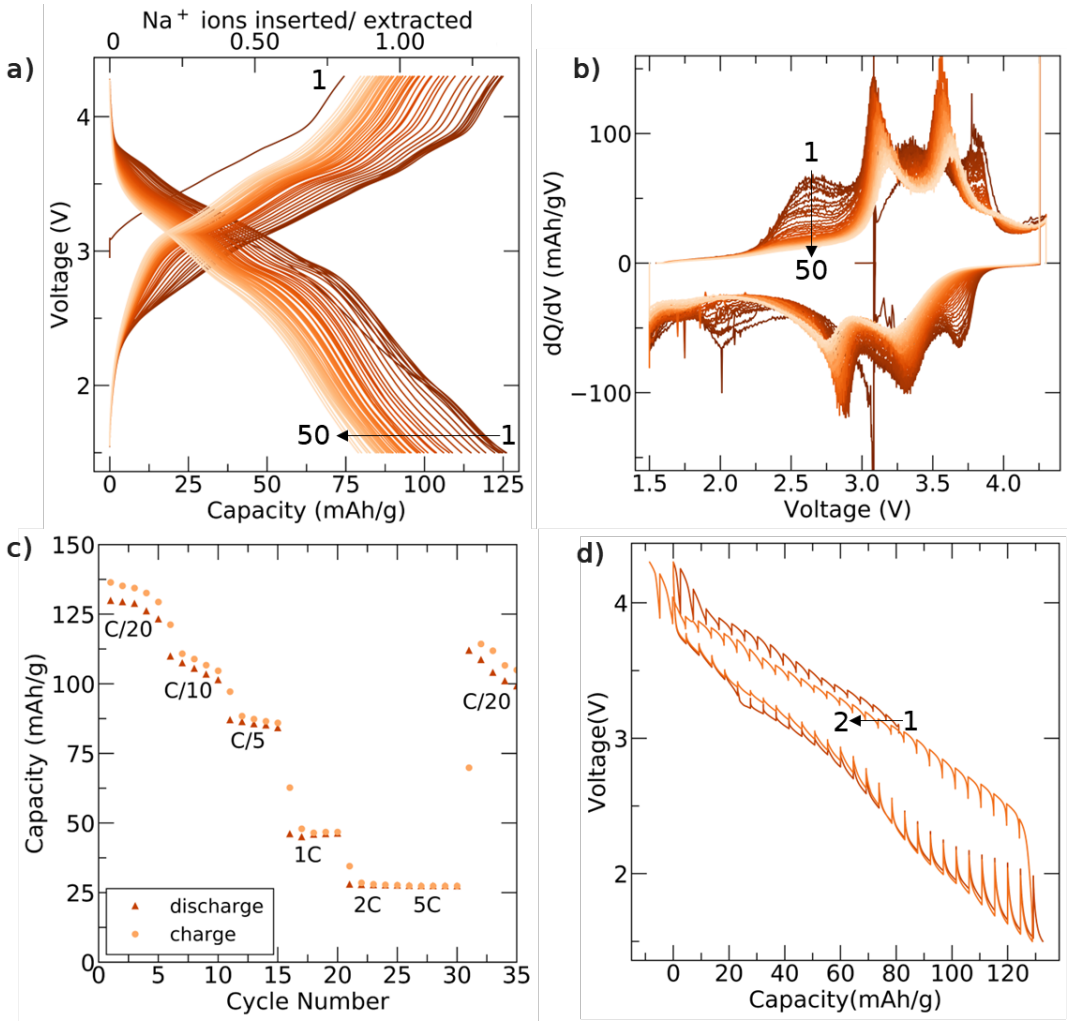

Figure 5. Electrochemical characterization of $Na_2Fe_2F_7$. **a)** Galvanostatic charge-discharge curves recorded at C/20 over the first 50 cycles, and **b)** corresponding differential capacity plots. **c)** Charge and discharge capacity obtained at various cycling rates and recorded over 35 cycles. The first charge step was omitted from the plot for clarity. **d)** Galvanostatic intermittent titration technique (GITT) data obtained over the first 2 cycles, where a 30-minute C/20 current pulse was applied followed by a 2-hour rest period. All the electrochemical results shown here were obtained using voltage cutoffs of 4.3 V and 1.5 V on charge and discharge, respectively.

Overall, the present $Na_2Fe_2F_7$ cathode exhibits respectable capacities over the first few cycles, but steady capacity fade upon extended cycling. These results differ from prior reports: Dey *et al.* reported a much lower initial reversible capacity of 58 mAh/g for a $Na_2Fe_2F_7$ cathode synthesized via a topochemical route,[36] while Park *et al.* obtained a higher initial capacity and higher cycling stability for a cathode prepared using a very similar synthesis route to the one adopted here.[30] While those discrepancies may stem from a different ratio of weberite variants in their samples, the electrochemical performance is likely also strongly dependent on the specific cathode preparation method used in each study. Such a strong dependence on electrode formulation and processing has been reported in poor electron conducting materials, such as transition metal fluoride electrodes for sodium-[41,50–53] and lithium-based[17,19,41] batteries, but also lithium iron phosphate.[42,54,55]

To better understand the origin of the capacity fade observed here, and the differences in the electrochemical performance reported in the three studies of $Na_2Fe_2F_7$, *ex situ* characterization of cathode samples and a computational investigation of the dependence of the electrochemical properties of weberite $Na_2Fe_2F_7$ on the structural variant are presented in the next sections.

Ex Situ Characterization of the Charge-Discharge Mechanism

The evolution of the dQ/dV features (**Figure 5b**) suggests a change in the bulk structure and redox mechanism of the $Na_2Fe_2F_7$ cathode upon extended cycling. To monitor those structural changes, *ex situ* SXRD and ^{23}Na ss-NMR characterization was performed on samples collected at the end of the 1st and 10th discharge, with results shown in **Figure 6**. Prior to cycling, weberite-type $Na_xFe_2F_7$ is the main active component of the cathode, with about 10 wt.% of Na_3FeF_6 present. However, *ex situ* SXRD data indicate a partial phase transformation of the $Na_xFe_2F_7$ weberite phase during cycling. Rietveld refinements of the SXRD patterns collected after the 1st and 10th cycle (see Rietveld refinement parameters listed in **Table S9** and **S10**) suggest that the newly formed phase is perovskite-like $NaFeF_3$ (*Pnma*), which accounts for 40 wt.% of the sample after the 1st discharge and 53 wt.% of the sample after the 10th discharge. A constant weight fraction of Na_3FeF_6 remains in the sample upon cycling, suggesting that the Na_yFeF_3 phase evolves at the expense of $Na_xFe_2F_7$ weberite phases only. Note that the unassigned impurity peaks are still present and do not evolve throughout cycling, suggesting that they correspond to an electrochemically-inactive component.

As SXRD is only sensitive to crystalline domains, ^{23}Na ss-NMR spectra were also collected on the *ex situ* samples, as shown in **Figure 6b**. For comparison, $NaFeF_3$ was synthesized – its crystal structure, laboratory XRD pattern, and corresponding refinement are shown in **Figure S9** – and its ^{23}Na ss-NMR spectrum is also shown in **Figure 6b**. The single, broad ^{23}Na signal at –118 ppm in the spectrum collected on $NaFeF_3$ presumably corresponds to the single, relatively symmetric Na environment in the perovskite-like structure. The NMR spectra collected on $Na_xFe_2F_7$ cathode samples reveal significant structural changes upon cycling, with the appearance of a signal at –118 ppm consistent with the formation of $NaFeF_3$. In line with the SXRD results, the fraction of $NaFeF_3$ increases with cycling, as indicated by the gradual growth of the –118 ppm peak. The broader and low intensity signals in the *ex situ* spectra likely correspond to cubic and bihexagonal pyramidal Na environments in residual $Na_xFe_2F_7$ domains, which can be differentiated using $\pi/2$ and $\pi/6$ flip angle spin echo experiments as discussed previously. Additionally, ^{19}F NMR data, shown in **Figure S10**, indicate a very minor NaF component in the *ex situ* samples. Integration of this signal suggests the presence of < 0.05 wt% of NaF in the total sample and thus this component is likely resulting from electrolyte decomposition[56,57] rather than from the phase transformation process.

Thus, our *ex situ* results show that our weberite cathode undergoes a phase transformation to Na_yFeF_3 ($0 \leq y \leq 1$) upon cycling. Those findings agree well with the electrochemical results, as Na_yFeF_3 is electrochemically active with very similar dQ/dV features and comparable experimental capacities ($\approx$ 105 mAh/g) as those observed on later cycles in **Figure 5b**.[58,59] Further, the several kinks observed in the galvanostatic data during the first discharge process may indicate the beginning of this phase transformation, as shown with select single cycle dQ/dV plots in **Figures S8c-f**. As the dQ/dV curve evolves at least to the 20th cycle, the $Na_xFe_2F_7$ to Na_yFeF_3 phase transformation continues up to this point. The electrochemical behavior on later cycles suggests that little to no weberite phase is left after 20 cycles, and the capacity observed is mostly due to Na (de)intercalation from/into Na_yFeF_3.

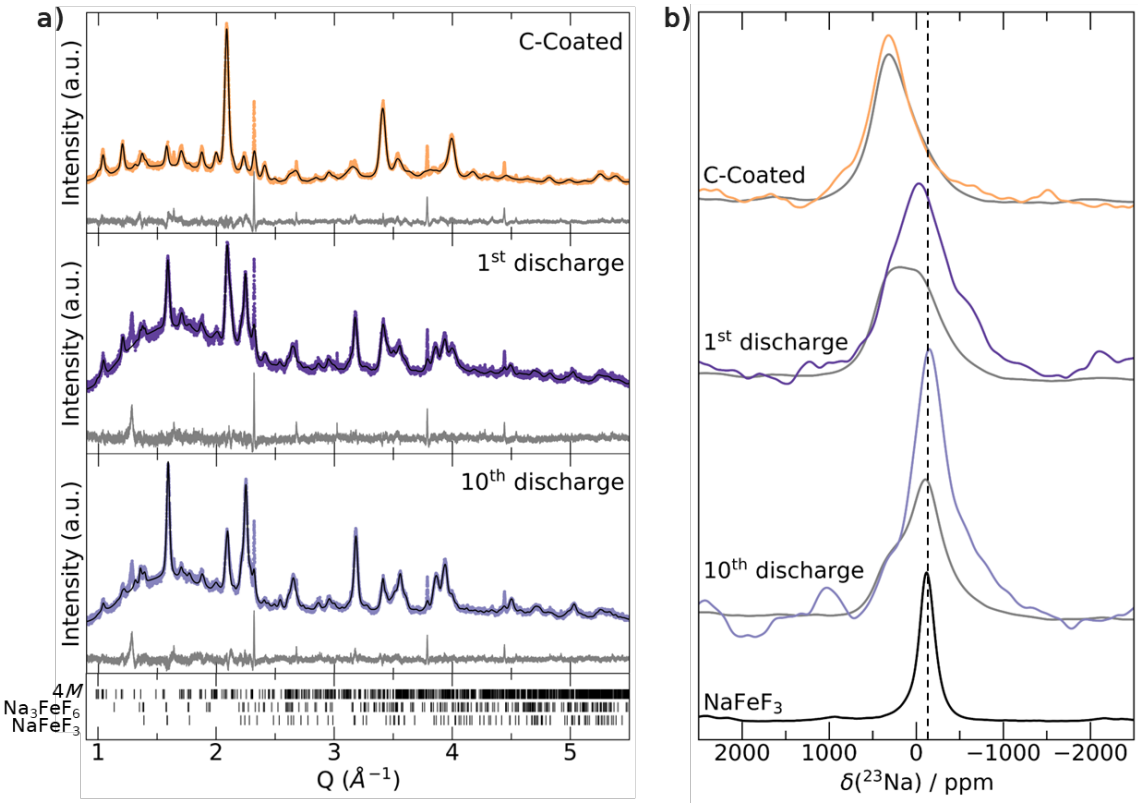

Figure 6, Characterization of ex situ $Na_xFe_2F_7$ cathode samples. **a)** SXRD patterns with corresponding Rietveld refinements (black, difference pattern in grey) and **b)** ^{23}Na ss-NMR spin echo spectra obtained on carbon-coated $Na_2Fe_2F_7$ (top), and on *ex situ* $Na_xFe_2F_7$ samples collected after the 1st (middle) and 10th (bottom) discharge. Spectra obtained with a $\pi/2$ excitation pulse are shown in grey, and those obtained with a $\pi/6$ excitation pulse are colored. The bottom ^{23}Na ss-NMR spectrum was obtained on $NaFeF_3$ using a $\pi/2$ pulse. The dashed line indicates the position of the $NaFeF_3$ resonance.

Based on the ternary phase diagram presented in **Figure 1d**, one would anticipate the as-synthesized $Na_2Fe_2F_7$ weberite cathode to decompose into FeF_2, $NaFeF_4$, and Na_3FeF_6. However, the black, dotted tie-line in the phase diagram represents the compositional evolution of the weberite at various stages of charge, clearly indicating that, on charge and discharge, thermodynamically-stable, perovskite-like Na_yFeF_3 phases (including FeF_3 and $NaFeF_3$) become possible decomposition phases of the metastable weberite cathode, providing a potential explanation for the observed phase transformation. While thermodynamics are important to rationalize phase transformations, kinetics must also be taken into account. Kinetic considerations may provide further insights into the mechanism of the phase transformation. Here, the perovskite-type Na_yFeF_3 and weberite $Na_xFe_2F_7$ structures contain similar building blocks, likely facilitating

the structural rearrangements. As previously mentioned, weberite $Na_xFe_2F_7$ contains a 3D network of corner-sharing FeF_6 octahedra, and 1D $Fe^{2+}F_6$ octahedral chains. Na_yFeF_3 similarly contains corner-sharing $Fe^{2+}F_6$ octahedral chains, now connected in 3D, as it forms a perovskite-like structure with Na occupying lattice sites in-between the chains (**Figure S9b**). Thus, upon Na (de)intercalation from/into the weberite structure, rearrangement of the FeF_6 octahedra may enable the weberite to perovskite phase transformation. Notably, Fe^{3+} possesses a high spin d^5 electron configuration, hence no octahedral vs. tetrahedral site preference, and can easily migrate to nearby sites as has been observed in other Fe-containing cathode materials.[60–63] Hence, the phase transformation is expected to be both kinetically facile and thermodynamically favored. Additional clues as to the onset and mechanism of the phase transformation come from the electrochemical, and *ex situ* SXRD and NMR analysis. First, the sharp and prominent dQ/dV feature observed at ~3.1 V during the first discharge process (**Figure 5b**) is tentatively attributed to the onset of the phase transformation, suggesting that this phase transformation initiates at a Na content $x < 2$ in the weberite phase. Given that the only two Na-containing phases observed by ^{23}Na NMR and SXRD in the discharged samples are the weberite and perovskite phases, and ^{19}F NMR data further confirms a negligible amount of NaF in these samples, the Na content in the perovskite phase formed on discharge is presumably equal to that in the initial weberite phase. Hence, a possible reaction mechanism is $Na_xFe_2F_7 \rightarrow 2\ Na_{x/2}FeF_3 + ½\ F_{2(g)}$, where $F_{2(g)}$ likely reacts with the electrolyte to form HF. In turn, HF formation during cycling could contribute to the rapid capacity decay. In fact, we have seen evidence of residues on the stainless steel plungers used in the Swagelok cells that are suggestive of corrosion.

The phase transformation observed here appears to be dependent on the specific weberite variant composition and/or the electrode preparation method, as Park *et al.* observed only the weberite phase via *ex situ* XRD after the 1000th cycle.[30] Regardless, the metastability and polymorphism of weberite compounds, exemplified here for $Na_2Fe_2F_7$, are important considerations for the development and accurate evaluation of this class of cathode materials.

Computational Investigation of the Electrochemical Properties of $Na_2Fe_2F_7$ Weberite Variants

To elucidate the influence of the weberite polymorph identity on the electrochemical performance of $Na_2Fe_2F_7$, the thermodynamic stability of a series of $Na_xFe_2F_7$ ($0 \leq x \leq 3$) compositions was evaluated from first principles for the 2*O*, 3*T*, and 4*M* variants. The three resulting convex hulls are overlaid in **Figure 7a**, which include various Na-vacancy orderings at intermediate $Na_xFe_2F_7$ compositions, and polymorph-specific Fe_2F_7 and $Na_3Fe_2F_7$ end-member phases (additional computational details are provided in **Note S3**). To achieve compositions with $x > 2$, additional Na intercalation sites were identified within the 2*O* and 4*M* $Na_2Fe_2F_7$ structures using bond valence sum mapping in the SoftBV software program,[64–66] as these polymorphs do not contain any intrinsic Na vacancies. The coordinates of possible intercalation sites are listed in **Table S11**. For the 3*T* structure with two half-filled Na sites at $x = 2$, no additional intercalation sites needed to be considered. The three variants have very similar energetics within the $0 \leq x \leq 3$ compositional range (differing by no more than 30 meV/atom), with the 3*T* structure being most stable overall, followed by the 4*M* variant. Notably, the presence of many intermediate $Na_xFe_2F_7$ compositions on the convex hulls (dashed lines), each with many Na-vacancy orderings within 10-20 meV/atom, suggests that all three weberite variants should undergo a solid solution mechanism leading to a sloped voltage profile (assuming that the weberite structure does not transform during cycling).

From those results, equilibrium voltage curves were generated for the three variants using the Nernst equation below,[67] where μ_{Na} is the chemical potential of Na in $Na_xFe_2F_7$, μ^{o}_{Na} is the Na chemical potential in the reference anode, and *e* is the elementary charge:

$$V = -\frac{\mu_{Na} - \mu_{Na}^{o}}{e}$$

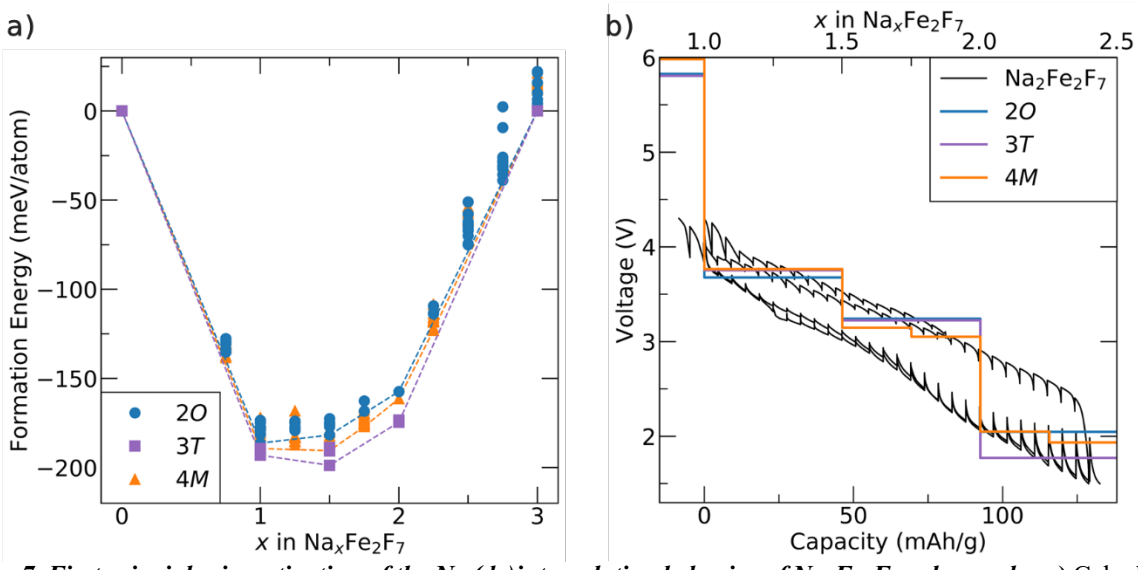

Figure 7, First principles investigation of the Na (de)intercalation behavior of $Na_2Fe_2F_7$ polymorphs. **a)** Calculated formation energies for 2*O*, 3*T*, and 4*M* $Na_xFe_2F_7$ structures. The convex hull for each polymorph is shown as a dashed line. **b)** Predicted voltage curves for the three weberite polymorphs derived from the 0 K $Na_xFe_2F_7$ formation energies shown in **a)**. The GITT data from **Figure 5d** has been reproduced in black for comparison.

Those equilibrium voltage curves are shown in **Figure 7b** along with the experimental $Na_2Fe_2F_7$ GITT data reproduced from **Figure 5d**. The computed curves are only an approximation to the true voltage curves as they are obtained from the 0 K DFT energies of intermediate $Na_xFe_2F_7$ phases, and as such neglect any temperature effects and assume that all intermediate phases have been correctly identified.[67] Here, the step-like voltage profiles obtained from first principles result from sampling over a small subset of intermediate $Na_xFe_2F_7$ compositions and Na/vacancy orderings, whereas the smoother, finite-temperature experimental profile is the result of entropic effects that create disorder on the Na sublattice. Overall, the predicted voltage profiles of the three polymorphs are very similar, with average voltages of 3.46, 3.49, and 3.43 V between $x = 1$ to 2 and of 2.75, 2.63, and 2.7 V between $x = 1$ to 3 for the 2*O*, 3*T*, and 4*M* polymorphs. In addition, the predicted profiles align well with experimental results. Below $x = 1$, large overpotentials are observed in the GITT data, which our DFT results suggest is due to the high potentials (> 5.75 V) required for further Na extraction, well outside the electrochemical stability window of conventional carbonate electrolytes.[68–70] The high predicted potentials at the top of charge arise from a rather unstable fully deintercalated structure, which is likely partly due to the difficulty of oxidizing Fe past Fe^{3+}.[71,72] In fact, Fe^{4+} has never been observed in fluoride materials. Large overpotentials are also observed in the GITT data at the end of discharge (x > 2), although our calculations suggest that Na should be able to intercalate up to $x = 3$ within the potential range used in our experiments. Thus, Na intercalation past x = 2 appears to be kinetically hindered in our experiments, which may in part be due to the large volume expansion (upwards of 10%) predicted past $x = 2$ (as shown in **Figure S11**), or by the phase transformation to $NaFeF_3$.

Overall, our DFT calculations predict a very similar electrochemical behavior for the three weberite structural variants, suggesting that the different layer stackings do not have a significant influence on the range of stoichiometries accessible via Na (de)intercalation. While we did not investigate the Na-ion conduction behavior within each polymorph, the slight structural variations between 2*O*, 3*T*, and 4*M* $Na_xFe_2F_7$ likely do not affect Na-ion transport drastically, especially considering that the Na polyhedral

connectivity is largely retained in each structural variant and the slow cycling rate used here (C/20). However, a more detailed study of the Na-ion transport properties of the three weberite variants is warranted.

While the origin of the very different electrochemical behaviors reported here and in Park *et al.*'s work[30] is difficult to ascertain, particularly since we are unable to compare the $Na_2Fe_2F_7$ polymorph ratios present in the starting cathodes due to the significant broadening of the diffraction patterns, we suspect that the different electrode preparation methods employed in the two studies play a large role, and kinetic limitations in our electrode films encourage a phase transformation to perovskite Na_yFeF_3 to occur, rather than topotactic Na intercalation. Thus, to prevent transformation of the weberite phase, these kinetic limitations must be overcome and/or the weberite phase must be stabilized with respect to competing phases.

Conclusions

This work comprises an in-depth examination of the structure, phase stability, and electrochemical performance of the $Na_2Fe_2F_7$ weberite cathode, using a combined experimental-computational approach. First principles calculations reveal that $Na_2Fe_2F_7$ is metastable and highly prone to polymorphism, as confirmed by Rietveld analysis of the synchrotron XRD data collected on the pristine $Na_2Fe_2F_7$ sample, indicating a mixture of the orthorhombic (2*O*), trigonal (3*T*), and monoclinic (4*M*) weberite polymorphs. Those results are consistent with the multiple Fe environments observed by ^{57}Fe Mössbauer spectroscopy, as well as the cubic and bihexagonal pyramidal Na environments identified by ^{23}Na solid-state NMR and first principles calculations of NMR parameters. The $Na_2Fe_2F_7$ cathode exhibits an initial reversible capacity of 125 mAh/g, and a 60% capacity retention after 50 cycles. Contributing to the capacity fade is a transformation of the $Na_2Fe_2F_7$ weberite phases to the Na_yFeF_3 perovskite, as revealed via *ex situ* synchrotron XRD and ^{23}Na solid-state NMR. A first principles investigation of the impact of polymorphism on the electrochemical performance reveals that the orthorhombic (2*O*), trigonal (3*T*), and monoclinic (4*M*) $Na_2Fe_2F_7$ polymorphs should behave similarly, transferring up to 2 Na between $Na_1Fe_2F_7$ to $Na_3Fe_2F_7$ at an average voltage of 2.7 V. Thus, from a thermodynamic standpoint, the polymorphic makeup of the $Na_2Fe_2F_7$ weberite cathode does not have a strong impact on the electrochemical behavior, although future investigations of the Na-ion transport properties of the weberite variants are warranted. We suspect that the poorer electrochemical performance of our $Na_2Fe_2F_7$ cathode compared to that reported in a previous study by Park *et al.* is largely due to differences in cathode film formulation and preparation methods. In this work, poorer overall kinetics hinder topotactic Na-ion (de)intercalation and favor a phase transformation reaction. Therefore, detailed reports regarding composite electrode preparation protocols and a careful analysis of the structure of weberite compounds are needed to assist the further development of this new class of Na-ion cathodes.

Methods

Material Synthesis –$Na_2Fe_2F_7$ was prepared via a mechanochemical-assisted solid-state route, using a stoichiometric mixture of dried binary fluoride precursors: NaF (Sigma-Aldrich, 99.99%), FeF_2 (Sigma-Aldrich, 99%), and FeF_3 (Sigma-Aldrich, 99.5%). All precursors and prepared materials were handled in an argon glovebox or else sealed under argon at all times as fluorides react readily with water to form hydrofluoric acid (HF). The precursors were hand-mixed and then 1 g of the powder was sealed in a 50 mL ZrO_2 ball mill jar with five 10 mm and ten 5 mm ZrO_2 balls and ball-milled at 400 rpm for 36 h to ensure homogenous mixing. The resultant powder was pelletized, annealed at 500°C for 30 min under an argon

flow, and then immediately quenched. To prevent air and water exposure, the quench was performed by using a long alumina tube that was shifted horizontally in the tube furnace following the anneal such that the pellet was no longer within the heating element. Subsequently, the alumina tube surrounding the pellet was flushed with room temperature nitrogen gas for 10 min. The pellet was then hand ground and the resulting powder used for all further characterization.

Material Characterization

X-ray Diffraction – High-resolution synchrotron powder diffraction patterns were collected on Beamline 11-BM at the Advanced Photon Source (APS), Argonne National Laboratory using an average wavelength of 0.458940 Å. Room temperature data were collected between 2θ of 0.5° and 50°. Resulting patterns were refined using first the Pawley method, to determine accurate peak shape fitting parameters, and then using the Rietveld method in TOPAS v7.[73] Crystal structures were depicted using VESTA 3.[74]

Scanning Electron Microscopy (SEM) – SEM images were obtained using a Thermo Fisher Apreo C LoVac SEM instrument with an accelerating voltage of 5 keV and current of 0.4 nA.

^{57}Fe Mössbauer Spectroscopy – Room temperature ^{57}Fe Mössbauer spectroscopy was performed using a SEECo Model W304 resonant gamma-ray spectrometer (activity = 60 mCi +/- 10%, ^{57}Co/Rh source) equipped with a Janis Research Model SVT-400 cryostat system. The source linewidth was < 0.12 mm s^{-1} for the innermost lines of a 25 μm α-Fe foil standard. Isomer shifts were referred to α-Fe foil at room temperature. All samples consisted of 15 to 20 mg of material loaded into a plastic holder in an Ar glovebox, coated with oil, capped, and then measured under a positive flow of N_2 at 305 K. The data were fit using MossA.[75]

Inductively Coupled Plasma Mass Spectrometry – Bulk chemical compositions were determined via ICP (Agilent 5800 ICP-OES). Samples were dissolved in a solution consisting of a 10:1 (v:v) ratio of 70% HNO_3 (Sigma-Aldrich) and concentrated HCl (Sigma-Aldrich).

^{23}Na Solid-State Nuclear Magnetic Resonance Spectroscopy (ssNMR) – ^{23}Na ssNMR data were collected on the $Na_2Fe_2F_7$ as-prepared and *ex situ* samples using a Bruker Avance 100 MHz (2.35 T) wide-bore NMR spectrometer with Larmor frequencies of 26.48 MHz at room temperature. The data were obtained at 60 kHz magic-angle spinning (MAS) using a 1.3 mm double-resonance HX probe. ^{23}Na NMR data were referenced against 1 M aqueous solutions of sodium chloride (NaCl, $\delta(^{23}Na) = 0$ ppm) and these samples were also used for pulse calibration. ^{23}Na spin echo spectra were acquired on all samples using π/2-π-π/2 and π/6-π/3-π/6 pulse sequences to selectively excite less quadrupolar environments and equally excite all environments, respectively. The radiofrequency (RF) pulse lengths were 0.125 μs for π/6, 0.25 μs for π/3, 0.375 μs for π/2, and 0.75 μs for π at a power of 62.5 W. A recycle delay between 30 ms to 80 ms was used to with the exact value optimized for each sample to ensure the full ^{23}Na signal was fully relaxed between pulses.

^{19}F Solid-State Nuclear Magnetic Resonance Spectroscopy (ssNMR) – ^{19}F ssNMR data were collected on the $Na_2Fe_2F_7$ *ex situ* samples using a Bruker Avance 100 MHz (2.35 T) wide-bore NMR spectrometer with Larmor frequencies of 94.08 MHz at room temperature. The data were obtained at 60 kHz magic-angle spinning (MAS) using a 1.3 mm double-resonance HX probe. ^{19}F NMR data were referenced against 1 M aqueous solutions of sodium fluoride (NaF, $\delta(^{19}F) = -118.14$ ppm) and these samples were also used for pulse calibration. The radiofrequency (RF) pulse lengths were 0.35 μs for π/2, and 0.7 μs for π. A recycle delay of 60 s was used for each sample to ensure the full ^{19}F signal was fully relaxed between pulses.

Electrochemical Characterization – The as-synthesized $Na_2Fe_2F_7$ materials were carbon-coated prior to electrochemical testing to form an electronically conductive carbon nanocomposite. The pristine materials

were combined with carbon black (Super C65, MTI Corporation) in a 7:2 ratio along with three 10 mm and three 5 mm ZrO_2 balls, in a 50 mL ZrO_2 ball mill jar and ball-milled at 300 rpm for 24 h. The resultant carbon-coated materials were hand ground for 30 min with 10 wt.% polytetrafluoroethylene (PTFE, Sigma-Aldrich), rolled into free-standing film electrodes, and punched into 6 mm disks with a loading density of 10 mg cm^{-2}. All electrochemical testing occurred in Swagelok-type cells against Na metal (Sigma) with a glass fiber separator (Whatman GF/D) using 200 µL of an in-house prepared electrolyte (< 20 ppm water content) of 1 M $NaPF_6$ (Strem Chemicals, 99%) in propylene carbonate (PC, Sigma, 99.7%) with 2 vol% fluoroethylene carbonate (FEC, Sigma-Aldrich, ≥ 99%).

Computational Details

Phase Stability & Energetics – Density functional theory (DFT) calculations were performed using the Vienna *ab initio* Simulation Package (VASP).[76–79] All VASP calculations used projector augmented wave (PAW) pseudopotentials (Na pv, Fe, and F),[80,81] a plane-wave energy cutoff of 520 eV, and the Perdew-Burke-Ernzerhof (PBE) generalized-gradient approximation (GGA)[82] functional with the Hubbard *U* correction.[83] A *U* value of 4 eV was used for Fe based on previous reports that have shown it to be broadly reliable for ionic solids.[84,85]

All calculations were performed on a 1x1x1 cell of the $Na_xFe_2F_7$ 2*O*, 3*T*, and 4*M* structures. For structures containing partial occupation of Na sites, symmetrically unique Na-vacancy orderings were enumerated and ranked according to their Ewald sum energy as implemented in Pymatgen[86] and only the three lowest energy structures considered. The structures were fully optimized (atomic positions and cell parameters), and the theoretical lattice parameters are compared to experimental values[30,36,37] in **Table S8**. To obtain accurate final energies, all relaxations were followed by a final static calculation. The convergence criteria were set as 10^{-5} eV for total energy and 0.01 eV/Å for the interatomic forces. Gaussian smearing with a width of 0.05 eV was used. All calculations were spin polarized with ferromagnetic ordering assumed. For the 2*O* and 3*T* structures, the Brillouin zone was sampled with a 4x3x4 and 6x6x3 k-point grid while the 4*M* structure used a reciprocal space discretization of 25 $Å^{-1}$.

Calculation of NMR Parameters – Spin-unrestricted hybrid density functional theory (DFT) / Hartree Fock (HF) calculations were performed using the CRYSTAL17 all-electron linear combination of atomic orbital code[87] to determine ^{23}Na NMR parameters for the $Na_2Fe_2F_7$ 2*O*, 3*T*, and 4*M* structures optimized in VASP, as described above, which were further relaxed in CRYSTAL. Two spin-polarized exchange-correlation functionals based upon the B3LYP form,[88–91] and with Fock exchange weights of $F_0 = 20\%$ (B3LYP or H20) and 35% (H35), were chosen for their good performance regarding the prediction of the electronic structure and band gaps of transition metal compounds (B3LYP or H20),[92,93] and for their accurate description of the magnetic properties of related compounds (H35).[94–96] All-electron atom-centered basis sets comprising fixed contractions of Gaussian primitive functions were employed throughout. Two types of basis sets were used: a smaller basis set (BS-I) was employed for structural optimizations, and a larger basis set (BS-II) was used for computing ^{23}Na NMR parameters which require an accurate description of the occupation of core-like electronic states. For BS-I, individual atomic sets are of the form (15*s*7*p*)/[1*s*3*sp*] for Na, (20*s*12*p*5*d*)/[1*s*4*sp*2*d*] for Fe, and (10*s*6*p*1*d*)/[4*s*3*p*1*d*] for F, where the values in parentheses denote the number of Gaussian primitives and the values in square brackets the contraction scheme. All BS-I sets were obtained from the CRYSTAL online repository and were unmodified from their previous use in a broad range of compounds.[97] For BS-II, a flexible and extended TSDP-derived (11*s*7*p*)/[7*s*3*p*] set for Na, an Ahlrichs DZP-derived[98] (13*s*9*p*5*d*)/[7*s*5*p*3*d*] set for Fe, and a modified IGLO-III and (10*s*6*p*2*d*)/[6*s*5*p*2*d*] set for F.

NMR parameters were computed on the fully optimized (atomic positions and cell parameters) $Na_2Fe_2F_7$ structures. All first principles structural optimizations were carried out in the ferromagnetic state on 1x1x1 cells (containing 44, 66, and 176 atoms for 2*O*, 3*T*, and 4*M* $Na_2Fe_2F_7$, respectively), after removal of all symmetry constraints and using the H20 and H35 hybrid functionals. Structural optimizations were pursued using the quasi-Newton algorithm with root-mean-square (RMS) convergence tolerances of 10^{-7}, 0.0003, and 0.0012 a.u. for total energy, RMS force, and RMS displacement, respectively. Tolerances for maximum force and displacement components were set to 1.5 times the respective RMS values. Sufficient convergence in total energies and spin densities was obtained by application of integral series truncation thresholds of 10^{-7}, 10^{-7}, 10^{-7}, 10^{-7}, and 10^{-14} for Coulomb overlap and penetration, exchange overlap, and g- and n-series exchange penetration, respectively as defined in the CRYSTAL17 documentation.[97] The final total energies and spin and charge distributions were obtained in the absence of any spin and eigenvalue constraints. NMR parameters were obtained on ferromagnetically aligned 2x1x2, 1x1x1, and 1x1x1 cells for 2*O*, 3*T*, and 4*M* $Na_2Fe_2F_7$, respectively, and on cells where one Fe spin was flipped using BS-II sets and a method described by Middlemiss *et al*.[99] Anisotropic Monkhorst-Pack reciprocal space meshes[100] with shrinking factors of 9 6 9 for 2*O*, 9 9 4 for 3*T*, and 9 6 3 for 4*M* were used throughout.

Conflicts of Interest

There are no conflicts of interest to declare.

Supporting Information

Crystal structure diagrams, simulated diffraction patterns, synthesis and electrochemical optimization results, Rietveld refinement results, Mossbauer fit parameters, ICP results, NMR calculation details and results, computational details and results, additional NMR and electrochemical data

Acknowledgements

This work made use of the shared facilities of the UC Santa Barbara MRSEC (DMR 1720256), a member of the Materials Research Facilities Network (www.mrfn.org) and the computational facilities administered by the Center for Scientific Computing at the CNSI and MRL facilities at UCSB (an NSF MRSEC; CNS 1725797, DMR 1720256). This work was supported by an NSF CAREER award under Award No. DMR 2141754. E.E.F. and V.C.W. were supported by the NSF Graduate Research Fellowship Program under Grant No. DGE 1650114. W.J. was supported by the RISE and FLAM internship programs through the MRSEC Program of the National Science Foundation under Award No. DMR 1720256. Synchrotron diffraction data were collected at beamlines 11-BM at the Advanced Photon Source, Argonne National Laboratory, a U.S. Department of Energy (DOE) Office of Science User Facility operated for the DOE Office of Science by Argonne National Laboratory under Contract No. DE-AC02-06CH11357. We gratefully acknowledge Dr. Hayden Evans for the helpful discussion regarding diffraction and data refinement as well as Dr. Raynald Giovine for helpful discussions on NMR spectroscopy.

References

(1) Clément, R. J.; Bruce, P. G.; Grey, C. P. Review-Manganese-Based P2-Type Transition Metal Oxides as Sodium-Ion Battery Cathode Materials. *Journal of the Electrochemical Society*. Electrochemical Society Inc. 2015, pp A2589–A2604. https://doi.org/10.1149/2.0201514jes.

(2) Rudola, A.; Rennie, A. J. R.; Heap, R.; Meysami, S. S.; Lowbridge, A.; Mazzali, F.; Sayers, R.; Wright, C. J.; Barker, J. Commercialisation of High Energy Density Sodium-Ion Batteries: Faradion's Journey and Outlook. *J. Mater. Chem. A* **2021**, *9* (13), 8279–8302. https://doi.org/10.1039/d1ta00376c.

(3) Yabuuchi, N.; Kajiyama, M.; Iwatate, J.; Nishikawa, H.; Hitomi, S.; Okuyama, R.; Usui, R.; Yamada, Y.; Komaba, S. P2-Type Nax[Fe1/2Mn1/2]O2 Made from Earth-Abundant Elements for Rechargeable Na Batteries. *Nat. Mater. 2012 116* **2012**, *11* (6), 512–517. https://doi.org/10.1038/nmat3309.

(4) Goodenough, J. B.; Hong, H. Y. P.; Kafalas, J. A. Fast Na+-Ion Transport in Skeleton Structures. *Mater. Res. Bull.* **1976**, *11* (2), 203–220. https://doi.org/10.1016/0025-5408(76)90077-5.

(5) Wu, V. C.; Giovine, R.; Foley, E. E.; Finzel, J.; Balasubramanian, M.; Sebti, E.; Mozur, E. M.; Kwon, A. H.; Clément, R. J. Unlocking New Redox Activity in Alluaudite Cathodes through Compositional Design. *Chem. Mater.* **2022**, *2022*, 50.

(6) Masquelier, C.; Croguennec, L. Polyanionic (Phosphates, Silicates, Sulfates) Frameworks as Electrode Materials for Rechargeable Li (or Na) Batteries. *Chem. Rev.* **2013**. https://doi.org/10.1021/cr3001862.

(7) Lu, Y.; Wang, L.; Cheng, J.; Goodenough, J. B. Prussian Blue: A New Framework of Electrode Materials for Sodium Batteries. *Chem. Commun.* **2012**, *48* (52), 6544–6546. https://doi.org/10.1039/c2cc31777j.

(8) Lim, C. Q. X.; Tan, Z. K. Prussian White with Near-Maximum Specific Capacity in Sodium-Ion Batteries. *ACS Appl. Energy Mater.* **2021**, *4* (6), 6214–6220. https://doi.org/10.1021/acsaem.1c00987.

(9) Tapia-Ruiz, N.; Armstrong, A. R.; Alptekin, H.; Amores, M. A.; Au, H.; Barker, J.; Boston, R.; Brant, W. R.; Brittain, J. M.; Chen, Y.; Chhowalla, M.; Choi, Y. S.; Costa, S. I. R.; Ribadeneyra, M. C.; Cussen, S. A.; Cussen, E. J.; David, W. I. F.; Desai, A. V.; Dickson, S. A. M.; Eweka, E. I.; Forero-Saboya, J. D.; Grey, C. P.; Griffin, J. M.; Gross, P.; Hua, X.; Irvine, J. T. S.; Johansson, P.; Jones, M. O.; Karlsmo, M.; Kendrick, E.; Kim, E.; Kolosov, O. V.; Li, Z.; Mertens, S. F. L.; Mogensen, R.; Monconduit, L.; Morris, R. E.; Naylor, A. J.; Nikman, S.; O'Keefe, C. A.; Ould, D. M. C.; Palgrave, R. G.; Poizot, P.; Ponrouch, A.; Renault, S.; Reynolds, E. M.; Rudola, A.; Sayers, R.; Scanlon, D. O.; Sen, S.; Seymour, V. R.; Silván, B.; Sougrati, M. T.; Stievano, L.; Stone, G. S.; Thomas, C. I.; Titirici, M. M.; Tong, J.; Wood, T. J.; Wright, D. S.; Younesi, R. 2021 Roadmap for Sodium-Ion Batteries. *J. Phys. Energy* **2021**, *3* (3), 031503. https://doi.org/10.1088/2515-7655/AC01EF.

(10) Lee, J.; Papp, J. K.; Clément, R. J.; Sallis, S.; Kwon, D.-H.; Shi, T.; Yang, W.; McCloskey, B. D.; Ceder, G. Mitigating Oxygen Loss to Improve the Cycling Performance of High Capacity Cation-Disordered Cathode Materials. *Nat. Commun.* **2017**, *8* (1), 981. https://doi.org/10.1038/s41467-017-01115-0.

(11) Clément, R. J.; Kitchaev, D.; Lee, J.; Gerbrand Ceder. Short-Range Order and Unusual Modes of Nickel Redox in a Fluorine-Substituted Disordered Rocksalt Oxide Lithium-Ion Cathode. *Chem. Mater.* **2018**, *30* (19), 6945–6956. https://doi.org/10.1021/acs.chemmater.8b03794.

(12) Huang, H.; Faulkner, T.; Barker, J.; Saidi, M. Y. Lithium Metal Phosphates, Power and

Automotive Applications. *J. Power Sources* **2009**, *189* (1), 748–751. https://doi.org/10.1016/J.JPOWSOUR.2008.08.024.

(13) Recham, N.; Chotard, J.-N.; Dupont, L.; Delacourt, C.; Walker, W.; Armand, M.; Tarascon, J.-M. A 3.6 V Lithium-Based Fluorosulphate Insertion Positive Electrode for Lithium-Ion Batteries. *Nat. Mater.* **2010**, *9* (1), 68–74. https://doi.org/10.1038/nmat2590.

(14) Nishijima, M.; Gocheva, I. D.; Okada, S.; Doi, T.; Yamaki, J. ichi; Nishida, T. Cathode Properties of Metal Trifluorides in Li and Na Secondary Batteries. *J. Power Sources* **2009**, *190* (2), 558–562. https://doi.org/10.1016/j.jpowsour.2009.01.051.

(15) Dimov, N.; Nishimura, A.; Chihara, K.; Kitajou, A.; Gocheva, I. D.; Okada, S. Transition Metal NaMF3 Compounds as Model Systems for Studying the Feasibility of Ternary Li-M-F and Na-M-F Single Phases as Cathodes for Lithium-Ion and Sodium-Ion Batteries. *Electrochim. Acta* **2013**, *110*, 214–220. https://doi.org/10.1016/j.electacta.2013.05.103.

(16) Amatucci, G. G.; Pereira, N. Fluoride Based Electrode Materials for Advanced Energy Storage Devices. *J. Fluor. Chem.* **2007**, *128* (4), 243–262. https://doi.org/10.1016/j.jfluchem.2006.11.016.

(17) Lemoine, K.; Hémon-Ribaud, A.; Leblanc, M.; Lhoste, J.; Tarascon, J. M.; Maisonneuve, V. Fluorinated Materials as Positive Electrodes for Li- and Na-Ion Batteries. *Chem. Rev.* **2022**, *122* (18), 14405–14439. https://doi.org/10.1021/acs.chemrev.2c00247.

(18) Li, H.; Zhou, H. Enhancing the Performances of Li-Ion Batteries by Carbon-Coating: Present and Future. *Chem. Commun.* **2012**, *48* (9), 1201–1217. https://doi.org/10.1039/C1CC14764A.

(19) Badway, F.; Pereira, N.; Cosandey, F.; Amatucci, G. G. Carbon-Metal Fluoride Nanocomposites: Structure and Electrochemistry of FeF3:C. *J. Electrochem. Soc.* **2003**, *150* (9), A1209. https://doi.org/10.1149/1.1596162.

(20) Li, C.; Gu, L.; Tong, J.; Maier, J. Carbon Nanotube Wiring of Electrodes for High-Rate Lithium Batteries Using an Imidazolium-Based Ionic Liquid Precursor as Dispersant and Binder: A Case Study on Iron Fluoride Nanoparticles. *ACS Nano* **2011**, *5* (4), 2930–2938. https://doi.org/10.1021/nn1035608.

(21) Ponrouch, A.; Cabana, J.; Dugas, R.; Slack, J. L.; Palacín, M. R. Electroanalytical Study of the Viability of Conversion Reactions as Energy Storage Mechanisms. *RSC Adv.* **2014**, *4* (68), 35988–35996. https://doi.org/10.1039/C4RA05189K.

(22) Wang, F.; Robert, R.; Chernova, N. A.; Pereira, N.; Omenya, F.; Badway, F.; Hua, X.; Ruotolo, M.; Zhang, R.; Wu, L.; Volkov, V.; Su, D.; Key, B.; Stanley Whittingham, M.; Grey, C. P.; Amatucci, G. G.; Zhu, Y.; Graetz, J. Conversion Reaction Mechanisms in Lithium Ion Batteries: Study of the Binary Metal Fluoride Electrodes. *J. Am. Chem. Soc.* **2011**, *133* (46), 18828–18836. https://doi.org/10.1021/ja206268a.

(23) Foley, E. E.; Wong, A.; Vincent, R. C.; Manche, A.; Zaveri, A.; Gonzalez-Correa, E.; Ménard, G.; Clément, R. J. Probing Reaction Processes and Reversibility in Earth-Abundant Na3FeF6 for Na-Ion Batteries. *Phys. Chem. Chem. Phys.* **2021**, *23* (36), 20052–20064. https://doi.org/10.1039/d1cp02763h.

(24) He, K.; Zhou, Y.; Gao, P.; Wang, L.; Pereira, N.; Amatucci, G. G.; Nam, K. W.; Yang, X. Q.; Zhu, Y.; Wang, F.; Su, D. Sodiation via Heterogeneous Disproportionation in FeF2 Electrodes for Sodium-Ion Batteries. *ACS Nano* **2014**, *8* (7), 7251–7259. https://doi.org/10.1021/nn502284y.

(25) Ni, D.; Fang, L.; Sun, W.; Shi, B.; Chen, X.; Li, H.; Wang, Z.; Sun, K. FeF2@MHCS Cathodes with High Capacity and Fast Sodium Storage Based on Nanostructure Construction. *ACS Appl. Energy Mater.* **2020**, *3* (11), 10340–10348. https://doi.org/10.1021/acsaem.0c00876.

(26) Zheng, Y.; Hwang, J.; Matsumoto, K.; Hagiwara, R. Electrochemical and Structural Behavior of Trirutile-Derived FeF3during Sodiation and Desodiation. *ACS Appl. Energy Mater.* **2022**, *5* (3), 3137–3145. https://doi.org/10.1021/ACSAEM.1C03756/ASSET/IMAGES/LARGE/AE1C03756_0007.JPEG.

(27) Arai, H.; Okada, S.; Sakurai, Y.; Yamaki, J. I. Cathode Performance and Voltage Estimation of Metal Trihalides. *J. Power Sources* **1997**, *68* (2), 716–719. https://doi.org/10.1016/S0378-7753(96)02580-3.

(28) Kitajou, A.; Ishado, Y.; Yamashita, T.; Momida, H.; Oguchi, T.; Okada, S. Cathode Properties of Perovskite-Type NaMF3 (M = Fe, Mn, and Co) Prepared by Mechanical Ball Milling for Sodium-Ion Battery. *Electrochim. Acta* **2017**, *245*, 424–429. https://doi.org/10.1016/J.ELECTACTA.2017.05.153.

(29) Gocheva, I. D.; Nishijima, M.; Doi, T.; Okada, S.; Yamaki, J. ichi; Nishida, T. Mechanochemical Synthesis of NaMF3 (M = Fe, Mn, Ni) and Their Electrochemical Properties as Positive Electrode Materials for Sodium Batteries. *J. Power Sources* **2009**, *187* (1), 247–252. https://doi.org/10.1016/j.jpowsour.2008.10.110.

(30) Park, H.; Lee, Y.; Cho, M.-K.; Kang, J.; Ko, W.; Jung, Y. H.; Jeon, T.-Y.; Hong, J.; Kim, H.; Myung, S.-T.; Kim, J. Na2Fe2F7: A Fluoride-Based Cathode for High Power and Long Life Na-Ion Batteries. *Energy Environ. Sci* **2021**, *14*, 1469–1479. https://doi.org/10.1039/d0ee02803g.

(31) Kang, J.; Ahn, J.; Park, H.; Ko, W.; Lee, Y.; Lee, S.; Lee, S.; Jung, S.-K.; Kim, J.; Kang, J.; Ahn, J.; Park, H.; Ko, W.; Lee, Y.; Lee, S.; Kim, J.; Jung, S.-K. Highly Stable Fe2+/Ti3+-Based Fluoride Cathode Enabling Low-Cost and High-Performance Na-Ion Batteries. *Adv. Funct. Mater.* **2022**, *32* (29), 2201816. https://doi.org/10.1002/ADFM.202201816.

(32) Liao, J.; Han, J.; Xu, J.; Du, Y.; Sun, Y.; Duan, L.; Zhou, X. Scalable Synthesis of Na2MVF7 (M = Mn, Fe, and Co) as High- Performance Cathode Materials for Sodium-Ion Batteries. *Chem. Commun.* **2021**, *57*, 11497–11500. https://doi.org/10.1039/D1CC04449D.

(33) Tressaud, A.; Dance, J. M.; Portier, J.; Hagenmuller, P. Interactions Magnetiques Dans Les Fluorures de Type Weberite. *Mat. Res. Bull* **1974**, *9* (9), 1219–1226.

(34) Cosier, R.; Wise, A.; Tressaud, A.; Grannec, J.; Olazcuaga, R.; Portier, J. Sur de Nouveaux Composés Fluorés Ferrimagnétiques à Structure Wébérite. *C. R. Hebd. Seances Acad. Sci. C* **1970**, *271*, 142–145.

(35) Euchner, H.; Clemens, O.; Reddy, M. A. Unlocking the Potential of Weberite-Type Metal Fluorides in Electrochemical Energy Storage. *npj Comput. Mater.* **2019**, *5* (1), 31. https://doi.org/10.1038/s41524-019-0166-3.

(36) Dey, U. K.; Barman, N.; Ghosh, S.; Sarkar, S.; Peter, S. C.; Senguttuvan, P. Topochemical Bottom-Up Synthesis of 2D- and 3D-Sodium Iron Fluoride Frameworks. *Chem. Mater.* **2019**, *31* (2), 295–299. https://doi.org/10.1021/acs.chemmater.8b04010.

(37) Yakubovich, O.; Urusov, V.; Massa, W.; Frenzen, G.; Babel, D. Structure of Na2Fe2F7 and Structural Relations in the Family of Weberites Na2MIIMIIIF7. *Zeitschrift für Anorg. und Allg. Chemie* **1993**, *619* (11), 1909–1919. https://doi.org/10.1002/zaac.19936191115.

(38) Grey, I. E.; Mumme, W. G.; Ness, T. J.; Roth, R. S.; Smith, K. L. Structural Relations between Weberite and Zirconolite Polytypes—Refinements of Doped 3T and 4M Ca2Ta2O7 and 3T CaZrTi2O7. *J. Solid State Chem.* **2003**, *174* (2), 285–295. https://doi.org/10.1016/S0022-4596(03)00222-6.

(39) Peschel, B.; Molinier, M.; Babel, D. Kristallstrukturbestimmungen an Vier Monoklinen Weberiten Na2MIIMIIIF7 (MII = Fe, Co; MIII = V, Cr). *Zeitschrift für Anorg. und Allg. Chemie* **1995**, *621*

(9), 1573–1581. https://doi.org/10.1002/zaac.19956210923.

(40) Dahlke, P.; Peschel, B.; Babel, D. Über Röntgenographische Einkristalluntersuchungen an Na2FeAlF7, Na2MIIGaF7 (MII = Ni, Zn) Und Na2ZnFeF7 Und Die Strukturchemie Der Weberite. *Zeitschrift für Anorg. und Allg. Chemie* **1998**, *624* (6), 1003–1010. https://doi.org/10.1002/(sici)1521-3749(199806)624:6<1003::aid-zaac1003>3.0.co;2-c.

(41) Badway, F.; Cosandey, F.; Pereira, N.; Amatucci, G. G. Carbon Metal Fluoride Nanocomposites: High-Capacity Reversible Metal Fluoride Conversion Materials as Rechargeable Positive Electrodes for Li Batteries. *J. Electrochem. Soc.* **2003**, *150* (10), A1318. https://doi.org/10.1149/1.1602454.

(42) Wang, J.; Sun, X. Understanding and Recent Development of Carbon Coating on LiFePO 4 Cathode Materials for Lithium-Ion Batteries. *Energy Environ. Sci.* **2012**, *5* (1), 5163–5185. https://doi.org/10.1039/C1EE01263K.

(43) Stephens, P. W. Phenomenological Model of Anisotropic Peak Broadening in Powder Diffraction. *J. Appl. Crystallogr.* **1999**, *32* (2), 281–289. https://doi.org/10.1107/S0021889898006001.

(44) Laligant, Y.; Calage, Y.; Heger, G.; Pannetier, J.; Ferey, G. Ordered Magnetic Frustration. VII. Na2NiFeF7: Reexamination of Its Crystal Structure in the True Space Group after Corrections from Renninger Effect and Refinement of Its Frustrated Magnetic Structure at 4.2 and 55 K. *J. Solid State Chem.* **1989**, *78* (1), 66–77. https://doi.org/10.1016/0022-4596(89)90128-X.

(45) Pebler, J.; Schmidt, K.; Babel, D.; Verscharen, W. Mössbauer-Spektroskopische Untersuchungen an Na2MnFeF7 / Mössbauer Spectroscopic Investigation of Na2MnFeF7. *Zeitschrift für Naturforsch. B* **2015**, *32* (4), 369–372. https://doi.org/10.1515/znb-1977-0403.

(46) Pankhurst, Q. A.; Johnson, C. E.; Wanklyn, B. M. A Mössbauer Study of Paramagnetic Na2MgFeF7. *J. Magn. Magn. Mater.* **1991**, *97* (1–3), 126–130. https://doi.org/10.1016/0304-8853(91)90170-F.

(47) Cai, L.; Nino, J. C. Complex Ceramic Structures. I. Weberites. *Acta Crystallogr. Sect. B Struct. Sci.* **2009**, *65* (3), 269–290. https://doi.org/10.1107/S0108768109011355.

(48) Wasylishen, R. E.; Ashbrook, S. E.; Wimperis, S. *NMR of Quadrupolar Nuclei in Solid Materials*; Wiley, Chichester, 2012.

(49) Bard, A. J.; Faulkner, L. R. *Electrochemical Methods*; Wiley, New York, 2001.

(50) Brennhagen, A.; Cavallo, C.; Wragg, D. S.; Vajeeston, P.; Sjåstad, A. O.; Koposov, A. Y.; Fjellvåg, H. Operando XRD Studies on Bi2MoO6as Anode Material for Na-Ion Batteries. *Nanotechnology* **2022**, *33* (18). https://doi.org/10.1088/1361-6528/ac4eb5.

(51) Yabuuchi, N.; Kubota, K.; Aoki, Y.; Komaba, S. Understanding Particle-Size-Dependent Electrochemical Properties of Li2MnO3-Based Positive Electrode Materials for Rechargeable Lithium Batteries. *J. Phys. Chem. C* **2016**, *120* (2), 875–885. https://doi.org/10.1021/acs.jpcc.5b10517.

(52) Jiang, C.; Wei, M.; Qi, Z.; Kudo, T.; Honma, I.; Zhou, H. Particle Size Dependence of the Lithium Storage Capability and High Rate Performance of Nanocrystalline Anatase TiO2 Electrode. *J. Power Sources* **2007**, *166* (1), 239–243. https://doi.org/10.1016/J.JPOWSOUR.2007.01.004.

(53) Li, C.; Gu, L.; Tong, J.; Maier, J. Carbon Nanotube Wiring of Electrodes for High-Rate Lithium Batteries Using an Imidazolium-Based Ionic Liquid Precursor as Dispersant and Binder: A Case Study on Iron Fluoride Nanoparticles. *ACS Nano* **2011**, *5* (4), 2930–2938. https://doi.org/10.1021/nn1035608.

(54) Belharouak, I.; Johnson, C.; Amine, K. Synthesis and Electrochemical Analysis of Vapor-

Deposited Carbon-Coated LiFePO4. *Electrochem. commun.* **2005**, *7* (10), 983–988. https://doi.org/10.1016/j.elecom.2005.06.019.

(55) Lepage, D.; Sobh, F.; Kuss, C.; Liang, G.; Schougaard, S. B. Delithiation Kinetics Study of Carbon Coated and Carbon Free LiFePO4. *J. Power Sources* **2014**, *256*, 61–65. https://doi.org/10.1016/J.JPOWSOUR.2013.12.054.

(56) Komaba, S.; Ishikawa, T.; Yabuuchi, N.; Murata, W.; Ito, A.; Ohsawa, Y. Fluorinated Ethylene Carbonate as Electrolyte Additive for Rechargeable Na Batteries. *ACS Appl. Mater. Interfaces* **2011**, *3* (11), 4165–4168. https://doi.org/10.1021/AM200973K/SUPPL_FILE/AM200973K_SI_001.PDF.

(57) Chen, L.; Kishore, B.; Walker, M.; Dancer, C. E. J.; Kendrick, E. Nanozeolite ZSM-5 Electrolyte Additive for Long Life Sodium-Ion Batteries. *Chem. Commun.* **2020**, *56* (78), 11609–11612. https://doi.org/10.1039/D0CC03976D.

(58) Martin, A.; Doublet, M.-L.; Kemnitz, E.; Pinna, N.; Martin, A.; Kemnitz, E.; Pinna, N.; Doublet, M. Reversible Sodium and Lithium Insertion in Iron Fluoride Perovskites. *Adv. Funct. Mater.* **2018**, *28* (29), 1802057. https://doi.org/10.1002/ADFM.201802057.

(59) Zheng, Y.; Jitto, S.; Hwang, J.; Matsumoto, K.; Hagiwara, R. Multiphase Transformation of NaFeF3 During Desodiation and Sodiation. *ACS Appl. Energy Mater.* **2022**. https://doi.org/10.1021/ACSAEM.2C02904.

(60) Lim, S. G.; Kwon, M. S.; Kim, T.; Kim, H.; Lee, S.; Lim, J.; Kim, H.; Lee, K. T. Correlation between the Cation Disorders of Fe3+and Li+in P3-Type Na0.67[Li0.1(Fe0.5Mn0.5)0.9]O2for Sodium Ion Batteries. *ACS Appl. Mater. Interfaces* **2022**, *14*, 33129. https://doi.org/10.1021/ACSAMI.2C05784/ASSET/IMAGES/LARGE/AM2C05784_0009.JPEG.

(61) Yabuuchi, N.; Yoshida, H.; Komaba, S. Crystal Structures and Electrode Performance of Alpha-NaFeO 2 for Rechargeable Sodium Batteries. *Electrochemistry* **2012**, *80* (10), 716–719. https://doi.org/10.5796/electrochemistry.80.716.

(62) Li, Y.; Gao, Y.; Wang, X.; Shen, X.; Kong, Q.; Yu, R.; Lu, G.; Wang, Z.; Chen, L. Iron Migration and Oxygen Oxidation during Sodium Extraction from NaFeO2. *Nano Energy* **2018**, *47*, 519–526. https://doi.org/10.1016/J.NANOEN.2018.03.007.

(63) Ye, T.; Barpanda, P.; Nishimura, S. I.; Furuta, N.; Chung, S. C.; Yamada, A. General Observation of Fe3+/Fe2+ Redox Couple Close to 4 v in Partially Substituted Li2FeP2O7 Pyrophosphate Solid-Solution Cathodes. *Chem. Mater.* **2013**, *25* (18), 3623–3629. https://doi.org/10.1021/CM401547Z/SUPPL_FILE/CM401547Z_SI_001.PDF.

(64) Chen, H.; Adams, S. Bond Softness Sensitive Bond-Valence Parameters for Crystal Structure Plausibility Tests. *IUCrJ* **2017**, *4* (5), 614–625. https://doi.org/10.1107/S2052252517010211/YC5011SUP1.PDF.

(65) Chen, H.; Wong, L. L.; Adams, S. SoftBV – a Software Tool for Screening the Materials Genome of Inorganic Fast Ion Conductors. *Acta Crystallogr. Sect. B Struct. Sci.* **2019**, *75* (1), 18–33. https://doi.org/10.1107/S2052520618015718.

(66) Wong, L. L.; Phuah, K. C.; Dai, R.; Chen, H.; Chew, W. S.; Adams, S. Bond Valence Pathway Analyzer-An Automatic Rapid Screening Tool for Fast Ion Conductors within SoftBV. *Chem. Mater.* **2021**, *33* (2), 625–641. https://doi.org/10.1021/ACS.CHEMMATER.0C03893/ASSET/IMAGES/LARGE/CM0C03893_0019.JPEG.

(67) Van Der Ven, A.; Deng, Z.; Banerjee, S.; Ong, S. P. Rechargeable Alkali-Ion Battery Materials: Theory and Computation. *Chem. Rev.* **2020**, *120* (14), 6977–7019.

https://doi.org/10.1021/acs.chemrev.9b00601.

(68) Yan, G.; Alves-Dalla-Corte, D.; Yin, W.; Madern, N.; Gachot, G.; Tarascon, J.-M. Assessment of the Electrochemical Stability of Carbonate-Based Electrolytes in Na-Ion Batteries. *J. Electrochem. Soc.* **2018**, *165* (7), A1222–A1230. https://doi.org/10.1149/2.0311807jes.

(69) Ponrouch, A.; Marchante, E.; Courty, M.; Tarascon, J.-M. M.; Palacín, M. R. In Search of an Optimized Electrolyte for Na-Ion Batteries. *Energy Environ. Sci.* **2012**, *5* (9), 8572. https://doi.org/10.1039/c2ee22258b.

(70) Liang, H. J.; Gu, Z. Y.; Zhao, X. X.; Guo, J. Z.; Yang, J. L.; Li, W. H.; Li, B.; Liu, Z. M.; Li, W. L.; Wu, X. L. Ether-Based Electrolyte Chemistry Towards High-Voltage and Long-Life Na-Ion Full Batteries. *Angew. Chemie Int. Ed.* **2021**, *60* (51), 26837–26846. https://doi.org/10.1002/ANIE.202112550.

(71) Li, B.; Sougrati, M. T.; Rousse, G.; Morozov, A. V.; Dedryvère, R.; Iadecola, A.; Senyshyn, A.; Zhang, L.; Abakumov, A. M.; Doublet, M. L.; Tarascon, J. M. Correlating Ligand-to-Metal Charge Transfer with Voltage Hysteresis in a Li-Rich Rock-Salt Compound Exhibiting Anionic Redox. *Nat. Chem.* **2021**, *13* (11), 1070–1080. https://doi.org/10.1038/s41557-021-00775-2.

(72) Fehse, M.; Bessas, D.; Mahmoud, A.; Diatta, A.; Hermann, R. P.; Stievano, L.; Sougrati, M. T. The Fe4+/3+ Redox Mechanism in NaFeO2: A Simultaneous Operando Nuclear Resonance and X-Ray Scattering Study. *Batter. Supercaps* **2020**, *3* (12), 1341–1349. https://doi.org/10.1002/BATT.202000157.

(73) Coelho, A. A. TOPAS and TOPAS-Academic: An Optimization Program Integrating Computer Algebra and Crystallographic Objects Written in C++. *J. Appl. Crystallogr.* **2018**, *51* (1), 210–218. https://doi.org/10.1107/S1600576718000183.

(74) Momma, K.; Izumi, F. VESTA 3 for Three-Dimensional Visualization of Crystal, Volumetric and Morphology Data. *J. Appl. Crystallogr.* **2011**, *44* (6), 1272–1276. https://doi.org/10.1107/S0021889811038970.

(75) Prescher, C.; McCammon, C.; Dubrovinsky, L. MossA: A Program for Analyzing Energy-Domain Mössbauer Spectra from Conventional and Synchrotron Sources. *J. Appl. Crystallogr.* **2012**, *45* (2), 329–331. https://doi.org/10.1107/S0021889812004979.

(76) Kresse, G.; Hafner, J. *Ab Initio* Molecular Dynamics for Liquid Metals. *Phys. Rev. B* **1993**, *47* (1), 558. https://doi.org/10.1103/PhysRevB.47.558.

(77) Kresse, G.; Hafner, J. *Ab Initio* Molecular-Dynamics Simulation of the Liquid-Metal–Amorphous-Semiconductor Transition in Germanium. *Phys. Rev. B* **1994**, *49* (20), 14251. https://doi.org/10.1103/PhysRevB.49.14251.

(78) Kresse, G.; Furthmüller, J. Efficiency of Ab-Initio Total Energy Calculations for Metals and Semiconductors Using a Plane-Wave Basis Set. *Comput. Mater. Sci.* **1996**, *6* (1), 15–50. https://doi.org/10.1016/0927-0256(96)00008-0.

(79) Kresse, G.; Furthmüller, J. Efficient Iterative Schemes for *Ab Initio* Total-Energy Calculations Using a Plane-Wave Basis Set. *Phys. Rev. B* **1996**, *54* (16), 11169. https://doi.org/10.1103/PhysRevB.54.11169.

(80) Blöchl, P. E. Projector Augmented-Wave Method. *Phys. Rev. B* **1994**, *50* (24), 17953. https://doi.org/10.1103/PhysRevB.50.17953.

(81) Kresse, G.; Joubert, D. From Ultrasoft Pseudopotentials to the Projector Augmented-Wave Method. *Phys. Rev. B* **1999**, *59* (3), 1758. https://doi.org/10.1103/PhysRevB.59.1758.

(82) Perdew, J. P.; Burke, K.; Ernzerhof, M. Generalized Gradient Approximation Made Simple. *Phys.*

Rev. Lett. **1996**, *77* (18), 3865–3868. https://doi.org/10.1103/PhysRevLett.77.3865.

(83) Anisimov, V. I.; Aryasetiawan, F.; Lichtenstein, A. I. First-Principles Calculations of the Electronic Structure and Spectra of Strongly Correlated Systems: The LDA+ U Method. *J. Phys. Condens. Matter* **1997**, *9* (4), 767. https://doi.org/10.1088/0953-8984/9/4/002.

(84) Jain, A.; Hautier, G.; Ong, S. P.; Moore, C. J.; Fischer, C. C.; Persson, K. A.; Ceder, G. Formation Enthalpies by Mixing GGA and GGA + U Calculations. *Phys. Rev. B - Condens. Matter Mater. Phys.* **2011**, *84* (4), 045115. https://doi.org/10.1103/PhysRevB.84.045115.

(85) Wang, L.; Maxisch, T.; Ceder, G. Oxidation Energies of Transition Metal Oxides within the GGA+ U Framework. *Phys. Rev. B* **2006**, *73*, 195107. https://doi.org/10.1103/PhysRevB.73.195107.

(86) Ong, S. P.; Richards, W. D.; Jain, A.; Hautier, G.; Kocher, M.; Cholia, S.; Gunter, D.; Chevrier, V. L.; Persson, K. A.; Ceder, G. Python Materials Genomics (Pymatgen): A Robust, Open-Source Python Library for Materials Analysis. *Comput. Mater. Sci.* **2013**, *68*, 314–319. https://doi.org/10.1016/J.COMMATSCI.2012.10.028.

(87) Dovesi, R.; Erba, A.; Orlando, R.; Zicovich-Wilson, C. M.; Civalleri, B.; Maschio, L.; Rérat, M.; Casassa, S.; Baima, J.; Salustro, S.; Kirtman, B. Quantum-Mechanical Condensed Matter Simulations with CRYSTAL. *Wiley Interdiscip. Rev. Comput. Mol. Sci.* **2018**, *8* (4), e1360. https://doi.org/10.1002/wcms.1360.

(88) Becke, A. D. A New Mixing of Hartree-Fock and Local Density-Functional Theories. *J. Chem. Phys.* **1993**, *98* (2), 1372–1377. https://doi.org/10.1063/1.464304.

(89) Lee, C.; Yang, W.; Parr, R. G. Development of the Colle-Salvetti Correlation-Energy Formula into a Functional of the Electron Density. *Phys. Rev. B* **1988**, *37* (2), 785–789. https://doi.org/10.1103/PhysRevB.37.785.

(90) Vosko, S. H.; Wilk, L.; Nusair, M. Accurate Spin-Dependent Electron Liquid Correlation Energies for Local Spin Density Calculations: A Critical Analysis. *Can. J. Phys.* **1980**, *58* (8), 1200–1211. https://doi.org/10.1139/p80-159.

(91) Stephens, P. J.; Devlin, F. J.; Chabalowski, C. F.; Frisch, M. J. Ab Initio Calculation of Vibrational Absorption and Circular Dichroism Spectra Using Density Functional Force Fields. *J. Phys. Chem.* **1994**, *98* (45), 11623–11627.

(92) Corà, F.; Alfredsson, M.; Mallia, G.; Middlemiss, D. S.; Mackrodt, W. C.; Dovesi, R.; Orlando, R. The Performance of Hybrid Density Functionals in Solid State Chemistry. In *Structure and Bonding*; Springer, Berlin, Heidelberg, 2012; Vol. 113, pp 171–232. https://doi.org/10.1007/b97944.

(93) Muscat, J.; Wander, A.; Harrison, N. M. On the Prediction of Band Gaps from Hybrid Functional Theory. *Chem. Phys. Lett.* **2001**, *342* (3–4), 397–401. https://doi.org/10.1016/S0009-2614(01)00616-9.

(94) Feng, X.; Harrison, N. M. Magnetic Coupling Constants from a Hybrid Density Functional with 35% Hartree-Fock Exchange. *Phys. Rev. B - Condens. Matter Mater. Phys.* **2004**, *70* (9), 092402. https://doi.org/10.1103/PhysRevB.70.092402.

(95) Middlemiss, D. S.; Lawton, L. M.; Wilson, C. C. A Solid-State Hybrid Density Functional Theory Study of Prussian Blue Analogues and Related Chlorides at Pressure. *J. Phys. Condens. Matter* **2008**, *20* (33), 335231. https://doi.org/10.1088/0953-8984/20/33/335231.

(96) de P. R. Moreira, I.; Illas, F.; Martin, R. L. Effect of Fock Exchange on the Electronic Structure and Magnetic Coupling in NiO. *Phys. Rev. B - Condens. Matter Mater. Phys.* **2002**, *65* (15),

1551021–15510214. https://doi.org/10.1103/PhysRevB.65.155102.

(97) Dovesi, R.; Erba, A.; Orlando, R.; Zicovich-Wilson, C. M.; Civalleri, B.; Maschio, L.; Rérat, M.; Casassa, S.; Baima, J.; Salustro, S.; Kirtman, B. CRYSTAL17 User's Manual. *WIREs Comput. Mol. Sci.* **2018**, *e1360*.

(98) Schäfer, A.; Horn, H.; Ahlrichs, R. Fully Optimized Contracted Gaussian Basis Sets for Atoms Li to Kr. *J. Chem. Phys.* **1992**, *97* (4), 2571–2577. https://doi.org/10.1063/1.463096.

(99) Middlemiss, D. S.; Ilott, A. J.; Clément, R. J.; Strobridge, F. C.; Grey, C. P. Density Functional Theory-Based Bond Pathway Decompositions of Hyperfine Shifts: Equipping Solid-State NMR to Characterize Atomic Environments in Paramagnetic Materials. *Chem. Mater.* **2013**, *25* (9), 1723–1734. https://doi.org/10.1021/cm400201t.

(100) Monkhorst, H. J.; Pack, J. D. Special Points for Brillouin-Zone Integrations. *Phys. Rev. B* **1976**, *13* (12), 5188–5192. https://doi.org/10.1103/PhysRevB.13.5188.

TOC Graphic

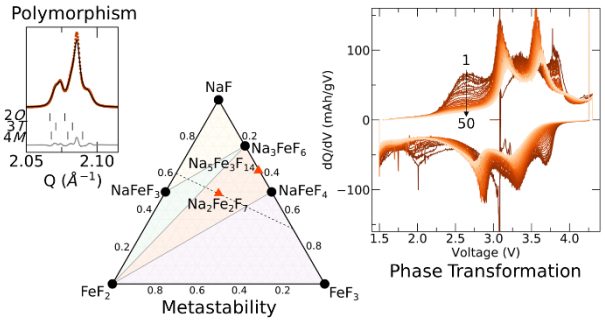
Polymorphism
2Q
3T
4M
2.05
2.10
Q (Å^{-1})
NaF
Na$_3$FeF$_6$
Na$_5$Fe$_3$F$_{14}$
NaFeF$_3$
NaFeF$_4$
Na$_2$Fe$_2$F$_7$
FeF$_2$
FeF$_3$
Metastability
dQ/dV (mAh/gV)
100
0
−100
1
50
1.5
2.0
2.5
3.0
3.5
4.0
Voltage (V)
Phase Transformation